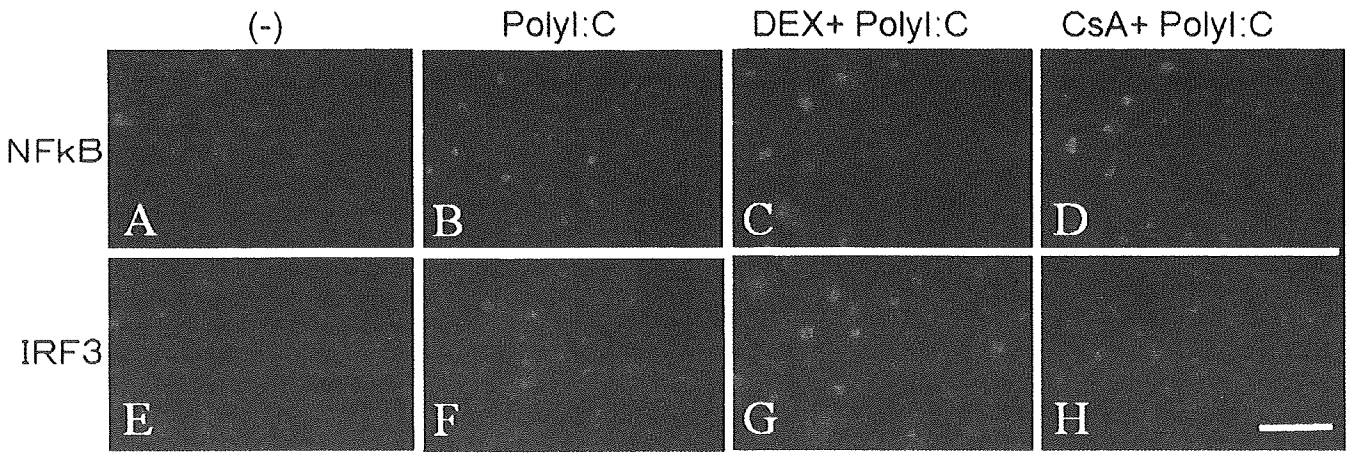

Figure 6. Immunohistochemical staining for NFκB and IRF3 in HCECs stimulated with poly(I:C) and cultured with or without of DEX or CsA for 24 h. NFκB p65 staining without poly(I:C, **A**), with poly(I:C, **B**), with DEX 10^{-5}M and poly(I:C, **C**), and with CsA 10^{-5}M and poly(I:C, **D**). IRF3 staining without poly(I:C, **E**), with poly(I:C, **F**), with DEX 10-5M and poly(I:C, **G**), and with CsA 10-5M and poly(I:C, **H**). Scale bar, 100 μm. Activated NFκB p65 and IRF-3 were clearly detected in the nuclei of most of cultured HCECs 3 h after stimulation by poly(I:C, **B** and **F**). In the presence of DEX, NFκB p65 and IRF-3 were detected in the nuclei of some HCECs but only in the cytosol of other HCECs (**C**, **G**). In the presence of CsA, NFκB p65 staining was detected in more HCEC nuclei after exposure to CsA than to DEX (D), while IRF3 was detected only in the nuclei of cultured HCECs (**H**).

responsive element (ISRE) is located on the human TLR3 promoter region, it has been suggested that IFNα/β induces the expression of TLR3 [42,43]. It has not been determined whether CsA regulates the IRFs or IFN, but our results showed no effect of CsA on IRF3 activation or on IFN-β production in HCECs.

The production of type I IFN is the first line of defense against viral infections, and it acts by limiting the early replication of viruses [19,20]. Deonarain et al. [21] demonstrated that IFN-β is crucial to this process because IFN-β-deficient mice were highly susceptible to viral infections. Our preliminary experiments showed that HSV infection was clearly depressed by poly(I:C) treatment prior to the HSV inoculation of the HCECs (data not shown). DEX treatment prior to HSV inoculation of HCECs led to the down-regulation of *TLR3* and *IFN-β* followed by increased *HSV-1* DNA and plaque formation. However, CsA did not interfere with the HSV-1 infection (data not shown). It is of interest to note that the anti-viral capabilities of corneal epithelial cells arise from their ability to produce IFN-β. Topical or systemic application of glucocorticoids results in the appearance of clinically active herpes keratitis, in which viral particles infect the corneal epithelial cells, leading to viral replication [9,10]. DEX has also been shown to increase the susceptibility of corneal epithelial cells to HSV-1 infection [44].

It has been known that TLR9 recognizes deoycytidylate-phosphate-deoxyguanosine (CpG) motifs in bacterial DNA, however, recent reports have demonstrated that TLR9 also recognizes CpG motifs in viral DNA, including HSV [24,45, 46]. In addition, retinoic acid-inducible gene (RIG)-I-like receptors (RLRs), including RIG-I, melanoma differentiation-associated gene 5 (Mda5), and *Leishmania* G-protein 2 (LGP2), have recently been identified as cytoplasmic proteins that recognize viral RNA [47,48]. The RLRs also activate NFκB and IRF3 following viral infection and poly(I:C) stimulation. RLRs-mediated signaling induced by dsRNA has been demonstrated in epidermal keratinocytes [49]. Our results showed an elevated production of inflammatory cytokines/chemokines that was associated with an up-regulated expression of TLR3, indicating that TLR3/TRIF signaling pathways are involved in the anti-viral response of HCECs. However, the presence of signaling cannot be fully accounted for by the TLR3/TRIF signaling pathway alone. It is possible that the TLR9 and RLRs pathways may also play a role in the production of inflammatory cytokines/ chemokines, but we did not study the RLRs pathway. Further investigation will be needed to determine the exact mechanisms.

In summary, we have demonstrated that HCECs have ability to produce inflammatory cytokines/chemokines via the innate immune system, and these responses can be modified by DEX and CsA. DEX down-regulated both NFκB and IRF3, whereas CsA down-regulated only NFκB. This inhibition by DEX of IRF3 followed by IFN-β production may be another mechanism in the immunosusceptibility of HCECs to HSV infection. Thus, the innate corneal immune system may be involved in HSV infection of HCECs, and further studies to determine the function of the innate immune system might lead to new therapeutic agents, or the development of effective ways of preventing corneal infections.

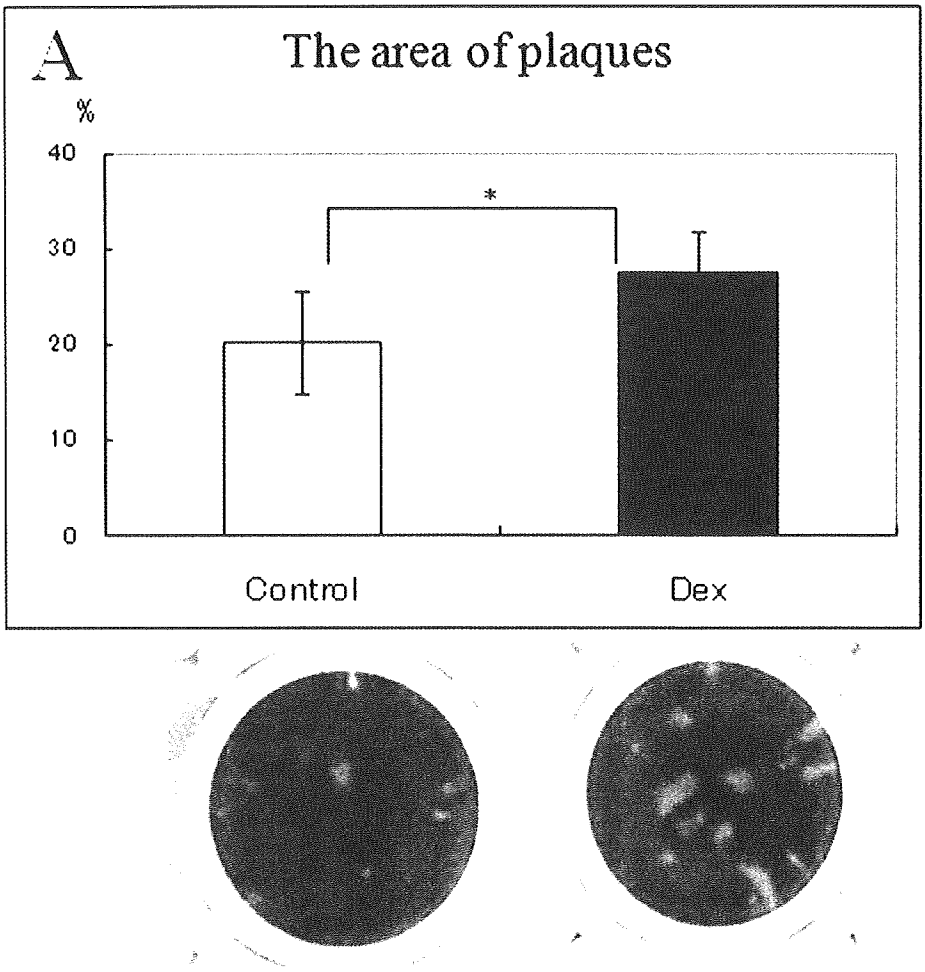

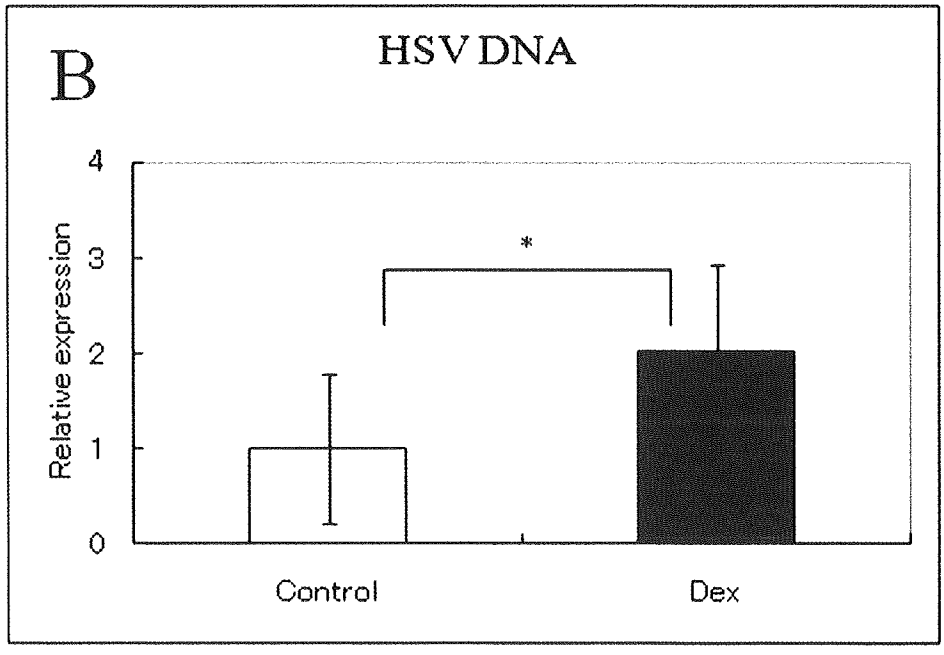

Figure 7. Effect of DEX and CsA on Herpes simplex virus 1 (HSV-1) infection. HCECs were cultured in the presence or absence of DEX (10^{-5} M), and inoculated with 50 MOI of HSV-1 for 48 h. The plaque area was increased when HCECs were pre-incubated with DEX (**A**). Real-time PCR results show a significantly higher level of *HSV-1* DNA in the supernatant with DEX (**B**). (*$p<0.05$)

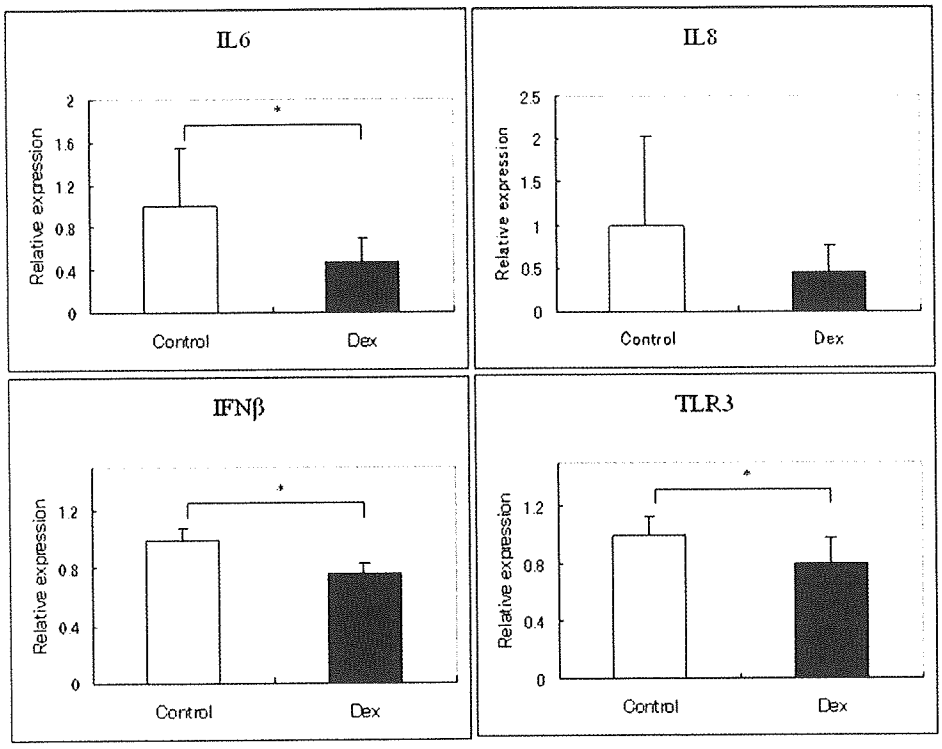

Figure 8. Effect of DEX and CsA on involvement of TLR3 signaling systems in HSV-1 infection of HCECs. HCECs were cultured in the presence or absence of DEX (10^{-5} M) and inoculated with 1,000 MOI of HSV-1 for 24 h. Real-time PCR shows that *IFN-β* and *TLR3* expression is down-regulated by DEX. *IL-6* and *IL-8* are also down-regulated, although the decrease of *IL-8* was not statistically significant. (*$p<0.05$)

ACKNOWLEDGMENTS

This work was supported by a Grant-in-Aid for Young Scientists (B) 19791273 from the Ministry of Education, Culture, Sports, Science, and Technology of Japan.

REFERENCES

1. Guillot L, Le Goffic R, Bloch S, Escriou N, Akira S, Chignard M, Si-Tahar M. Involvement of Toll-like Receptor 3 in the Immune Response of Lung Epithelial Cells to Double-stranded RNA and Influenza A Virus. J Biol Chem 2005; 280:5571-80. [PMID: 15579900]
2. Muir A, Soong G, Sokol S, Reddy B, Gomez MI, Van Heeckeren A, Prince A. Toll-like receptors in normal and cystic fibrosis airway epithelial cells. Am J Respir Cell Mol Biol 2004; 30:777-83. [PMID: 14656745]
3. Baker BS, Ovigne JM, Powles AV, Corcoran S, Fry L. Normal keratinocytes express Toll-like receptors (TLRs) 1, 2 and 5: modulation of TLR expression in chronic plaque psoriasis. Br J Dermatol 2003; 148:670-9. [PMID: 12752123]
4. Pivarcsi A, Bodai L, Rethi B, Kenderessy-Szabo A, Koreck A, Szell M, Beer Z, Bata-Csorgoo Z, Magocsi M, Rajnavolgyi E, Dobozy A, Kemeny L. Expression and function of Toll-like receptors 2 and 4 in human keratinocytes. Int Immunol 2003; 15:721-30. [PMID: 12750356]
5. Cario E, Podolsky DK. Differential alteration in intestinal epithelial cell expression of toll-like receptor 3 (TLR3) and TLR4 in inflammatory bowel disease. Infect Immun 2000; 68:7010-7. [PMID: 11083826]
6. Schaefer TM, Desouza K, Fahey JV, Beagley KW, Wira CR. Toll-like receptor (TLR) expression and TLR-mediated cytokine/chemokine production by human uterine epithelial cells. Immunology 2004; 112:428-36. [PMID: 15196211]
7. Ueta M, Hamuro J, Kiyono H, Kinoshita S. Triggering of TLR3 by polyI:C in human corneal epithelial cells to induce inflammatory cytokines. Biochem Biophys Res Commun 2005; 331:285-94. [PMID: 15845391]
8. Li J, Shen J, Beuerman RW. Expression of toll-like receptors in human limbal and conjunctival epithelial cells. Mol Vis 2007; 13:813-22. [PMID: 17615542]
9. Leopold IH, Sery TW. Epidemiology of Herpes Simplex Keratitis. Invest Ophthalmol 1963; 2:498-503. [PMID: 14069759]
10. McGill J, Fraunfelder FT, Jones BR. Current and proposed management of ocular herpes simplex. Surv Ophthalmol 1976; 20:358-65. [PMID: 817407]
11. Wilhelmus KR, Coster DJ, Donovan HC, Falcon MG, Jones BR. Prognosis indicators of herpetic keratitis. Analysis of a five-year observation period after corneal ulceration. Arch Ophthalmol 1981; 99:1578-82. [PMID: 6793030]
12. Schaefer TM, Fahey JV, Wright JA, Wira CR. Innate immunity in the human female reproductive tract: antiviral response of uterine epithelial cells to the TLR3 agonist poly[I:C]. J Immunol 2005; 174:992-1002. [PMID: 15634923]
13. Sha Q, Truong-Tran AQ, Plitt JR, Beck LA, Schleimer RP. Activation of airway epithelial cells by toll-like receptor agonists. Am J Respir Cell Mol Biol 2004; 31:358-64. [PMID: 15191912]
14. Akira S, Uematsu S, Takeuchi O. Pathogen recognition and innate immunity. Cell 2006; 124:783-801. [PMID: 16497588]
15. Oshiumi H, Matsumoto M, Funami K, Akazawa T, Seya T. TICAM-1, an adaptor molecule that participates in Toll-like receptor 3-mediated interferon-beta induction. Nat Immunol 2003; 4:161-7. [PMID: 12539043]

16. Yamamoto M, Sato S, Hemmi H, Hoshino K, Kaisho T, Sanjo H, Takeuchi O, Sugiyama M, Okabe M, Takeda K, Akira S. Role of adaptor TRIF in the MyD88-independent toll-like receptor signaling pathway. Science 2003; 301:640-3. [PMID: 12855817]
17. Alexopoulou L, Holt AC, Medzhitov R, Flavell RA. Recognition of double-stranded RNA and activation of NF-kappaB by Toll-like receptor 3. Nature 2001; 413:732-8. [PMID: 11607032]
18. Yamamoto M, Sato S, Mori K, Hoshino K, Takeuchi O, Takeda K, Akira S. Cutting edge: a novel Toll/IL-1 receptor domain-containing adapter that preferentially activates the IFN-beta promoter in the Toll-like receptor signaling. J Immunol 2002; 169:6668-72. [PMID: 12471095]
19. Muller U, Steinhoff U, Reis LF, Hemmi S, Pavlovic J, Zinkernagel RM, Aguet M. Functional role of type I and type II interferons in antiviral defense. Science 1994; 264:1918-21. [PMID: 8009221]
20. Poli G, Biswas P, Fauci AS. Interferons in the pathogenesis and treatment of human immunodeficiency virus infection. Antiviral Res 1994; 24:221-33. [PMID: 7526793]
21. Deonarain R, Alcami A, Alexiou M, Dallman MJ, Gewert DR, Porter AC. Impaired antiviral response and alpha/beta interferon induction in mice lacking beta interferon. J Virol 2000; 74:3404-9. [PMID: 10708458]
22. Jacobs BL, Langland JO. When two strands are better than one: the mediators and modulators of the cellular responses to double-stranded RNA. Virology 1996; 219:339-49. [PMID: 8638399]
23. Kariko K, Ni H, Capodici J, Lamphier M, Weissman D. mRNA is an endogenous ligand for Toll-like receptor 3. J Biol Chem 2004; 279:12542-50. [PMID: 14729660]
24. Ashkar AA, Yao XD, Gill N, Sajic D, Patrick AJ, Rosenthal KL. Toll-like receptor (TLR)-3, but not TLR4, agonist protects against genital herpes infection in the absence of inflammation seen with CpG DNA. J Infect Dis 2004; 190:1841-9. [PMID: 15499542]
25. Hayashi K, Hooper LC, Chin MS, Nagineni CN, Detrick B, Hooks JJ. Herpes simplex virus 1 (HSV-1) DNA and immune complex (HSV-1-human IgG) elicit vigorous interleukin 6 release from infected corneal cells via Toll-like receptors. J Gen Virol 2006; 87:2161-9. [PMID: 16847112]
26. World Medical Association declaration of Helsinki. Recommendations guiding physicians in biomedical research involving human subjects. JAMA 1997; 277:925-6. [PMID: 9062334]
27. Morita S, Shirakata Y, Shiraishi A, Kadota Y, Hashimoto K, Higashiyama S, Ohashi Y. Human corneal epithelial cell proliferation by epiregulin and its cross-induction by other EGF family members. Mol Vis 2007; 13:2119-28. [PMID: 18079685]
28. Rutledge RG, Cote C. Mathematics of quantitative kinetic PCR and the application of standard curves. Nucleic Acids Res 2003; 31:e93. [PMID: 12907745]
29. Arici A, Head JR, MacDonald PC, Casey ML. Regulation of interleukin-8 gene expression in human endometrial cells in culture. Mol Cell Endocrinol 1993; 94:195-204. [PMID: 8224523]
30. Jiang Y, Beller DI, Frendl G, Graves DT. Monocyte chemoattractant protein-1 regulates adhesion molecule expression and cytokine production in human monocytes. J Immunol 1992; 148:2423-8. [PMID: 1348518]
31. Taub DD, Conlon K, Lloyd AR, Oppenheim JJ, Kelvin DJ. Preferential migration of activated CD4+ and CD8+ T cells in response to MIP-1 alpha and MIP-1 beta. Science 1993; 260:355-8. [PMID: 7682337]
32. Limberg M, Bugge C. Tear concentrations of topically applied ciprofloxacin. Cornea 1994; 13:496-9. [PMID: 7842707]
33. Scuderi AC, De Lazzari A, Miano F, Zola P. Residence time of netilmicin in tears. Cornea 2002; 21:48-50. [PMID: 11805507]
34. Imai E, Miner JN, Mitchell JA, Yamamoto KR, Granner DK. Glucocorticoid receptor-cAMP response element-binding protein interaction and the response of the phosphoenolpyruvate carboxykinase gene to glucocorticoids. J Biol Chem 1993; 268:5353-6. [PMID: 8449898]
35. Mukaida N, Morita M, Ishikawa Y, Rice N, Okamoto S, Kasahara T, Matsushima K. Novel mechanism of glucocorticoid-mediated gene repression. Nuclear factor-kappa B is target for glucocorticoid-mediated interleukin 8 gene repression. J Biol Chem 1994; 269:13289-95. [PMID: 8175759]
36. Ray A, Prefontaine KE. Physical association and functional antagonism between the p65 subunit of transcription factor NF-kappa B and the glucocorticoid receptor. Proc Natl Acad Sci USA 1994; 91:752-6. [PMID: 8290595]
37. Yang-Yen HF, Chambard JC, Sun YL, Smeal T, Schmidt TJ, Drouin J, Karin M. Transcriptional interference between c-Jun and the glucocorticoid receptor: mutual inhibition of DNA binding due to direct protein-protein interaction. Cell 1990; 62:1205-15. [PMID: 2169352]
38. Sigal NH, Dumont FJ, Cyclosporin A. FK-506, and rapamycin: pharmacologic probes of lymphocyte signal transduction. Annu Rev Immunol 1992; 10:519-60. [PMID: 1375473]
39. Kalli K, Huntoon C, Bell M, McKean DJ. Mechanism responsible for T-cell antigen receptor- and CD28- or interleukin 1 (IL-1) receptor-initiated regulation of IL-2 gene expression by NF-kappaB. Mol Cell Biol 1998; 18:3140-8. [PMID: 9584155]
40. Marienfeld R, Neumann M, Chuvpilo S, Escher C, Kneitz B, Avots A, Schimpl A, Serfling E. Cyclosporin A interferes with the inducible degradation of NF-kappa B inhibitors, but not with the processing of p105/NF-kappa B1 in T cells. Eur J Immunol 1997; 27:1601-9. [PMID: 9247567]
41. Reily MM, Pantoja C, Hu X, Chinenov Y, Rogatsky I. The GRIP1:IRF3 interaction as a target for glucocorticoid receptor-mediated immunosuppression. EMBO J 2006; 25:108-17. [PMID: 16362036]
42. Heinz S, Haehnel V, Karaghiosoff M, Schwarzfischer L, Muller M, Krause SW, Rehli M. Species-specific regulation of Toll-like receptor 3 genes in men and mice. J Biol Chem 2003; 278:21502-9. [PMID: 12672806]
43. Tanabe M, Kurita-Taniguchi M, Takeuchi K, Takeda M, Ayata M, Ogura H, Matsumoto M, Seya T. Mechanism of up-regulation of human Toll-like receptor 3 secondary to infection of measles virus-attenuated strains. Biochem Biophys Res Commun 2003; 311:39-48. [PMID: 14575692]
44. Weinstein BI, Schwartz J, Gordon GG, Dominguez MO, Varma S, Dunn MW, Southren AL. Characterization of a glucocorticoid receptor and the direct effect of

dexamethasone on herpes simplex virus infection of rabbit corneal cells in culture. Invest Ophthalmol Vis Sci 1982; 23:651-9. [PMID: 7129809]

45. Ashkar AA, Bauer S, Mitchell WJ, Vieira J, Rosenthal KL. Local delivery of CpG oligodeoxynucleotides induces rapid changes in the genital mucosa and inhibits replication, but not entry, of herpes simplex virus type 2. J Virol 2003; 77:8948-56. [PMID: 12885911]
46. Harandi AM. The potential of immunostimulatory CpG DNA for inducing immunity against genital herpes: opportunities and challenges. J Clin Virol 2004; 30:207-10. [PMID: 15135735]
47. Meylan E, Tschopp J. Toll-like receptors and RNA helicases: two parallel ways to trigger antiviral responses. Mol Cell 2006; 22:561-9. [PMID: 16762830]
48. Yoneyama M, Fujita T. Function of RIG-I-like receptors in antiviral innate immunity. J Biol Chem 2007; 282:15315-8. [PMID: 17395582]
49. Kalali BN, Kollisch G, Mages J, Muller T, Bauer S, Wagner H, Ring J, Lang R, Mempel M, Ollert M. Double-stranded RNA induces an antiviral defense status in epidermal keratinocytes through TLR3-, PKR-, and MDA5/RIG-I-mediated differential signaling. J Immunol 2008; 181:2694-704. [PMID: 18684960]

The print version of this article was created on 3 May 2009. This reflects all typographical corrections and errata to the article through that date. Details of any changes may be found in the online version of the article.

Molecular Vision 2009; 15:974-979 <http://www.molvis.org/molvis/v15/a102>
Received 5 August 2008 | Accepted 10 May 2009 | Published 15 May 2009

Double mutation (R124H, N544S) of *TGFBI* in two sisters with combined expression of Avellino and lattice corneal dystrophies

Naoyuki Yamada,[1] Koji Kawamoto,[1] Naoyuki Morishige,[1] Tai-ichiro Chikama,[2] Teruo Nishida,[1] Mitsuaki Nishioka,[3] Naoko Okayama,[3] Yuji Hinoda[3]

[1]Department of Ophthalmology, Yamaguchi University Graduate School of Medicine, Ube City, Yamaguchi, Japan; [2]Department of Ocular Pathophysiology, Yamaguchi University School of Medicine, Ube City, Yamaguchi, Japan; [3]Division of Laboratory, Yamaguchi University Hospital, Ube City, Yamaguchi, Japan

Purpose: The R124H mutation of the keratoepithelin gene (*TGFBI*) causes Avellino corneal dystrophy whereas the N544S mutation of this same gene gives rise to lattice corneal dystrophy. We now report two cases with both R124H and N544S mutations of *TGFBI*.

Methods: Genomic DNA and cDNA were isolated from the proband and family members and were subjected to polymerase chain reaction–mediated amplification of exons 1–17 of *TGFBI*. The amplification products were directly sequenced. Allele-specific cloning and sequencing were applied to evaluate the compound heterozygous mutation.

Results: Molecular genetic analysis revealed that the proband and one sister harbored both a heterozygous CGC→CAC (Arg→His) mutation at codon 124 and a heterozygous AAT→AGT (Asn→Ser) mutation at codon 544 of *TGFBI*. Slit-lamp examination revealed multiple granular regions of opacity and lattice lines in the corneal stroma of the proband and her sister with the double mutation. Allele-specific cloning and sequencing revealed that the R124H and N544S mutations are on different chromosomes.

Conclusions: As far as we are aware, this is the first report of a patient with a double mutation (R124H, N544S) of *TGFBI* causing an autosomal dominant form of corneal dystrophy. The clinical manifestations of the two cases with both R124H and N544S mutations appeared to be a summation of Avellino and lattice corneal dystrophies.

Mutations of the keratoepithelin gene (*TGFBI*) are responsible for most corneal dystrophies. *TGFBI* was first identified as a transforming growth factor-β1 (TGF-β1)-inducible gene in a human lung adenocarcinoma cell line [1]. The point mutations R124C, R124H, R555W, and R555Q of *TGFBI* were initially found to give rise to lattice corneal dystrophy (LCD), Avellino corneal dystrophy (ACD), Groenouw type I corneal dystrophy, and Reis-Bücklers corneal dystrophy, respectively [2]. Many additional mutations of *TGFBI* were subsequently found to be responsible for autosomal dominant corneal dystrophies [3, 4]. ACD is characterized by the presence of granular and linear opacities in the corneal stroma. The deposits in the corneal stroma of patients with ACD are of a hyaline and amyloid nature. The only identified mutation associated with ACD is R124H of *TGFBI* [2]. LCD is an inherited form of amyloidosis that is characterized by the development of lattice lines and opacities in the cornea. Several distinct mutations of *TGFBI* including R124C [2], L518P [5], P501T [6], L527R [7], N544S [8], A546T [9], and N622K (T1913G or T1913A) [3] have been associated with LCD. LCD is classified clinically into several subtypes [3,4], but standardized definitions of each subtype have not been achieved to date. The subtype of LCD caused by the N544S mutation of *TGFBI* is characterized by tiny nodular deposits with thin lattice lines in the middle portion of the corneal stroma [10].

Several case reports have suggested that corneal dystrophies caused by homozygous point mutations of *TGFBI* are characterized by an earlier onset, more severe symptoms, and a higher frequency of recurrence after keratoplasty compared with those attributable to the corresponding heterozygous mutations [11-15]. A few case reports have also described individuals with corneal dystrophy who harbor two distinct mutations in *TGFBI*, the membrane component, chromosome 1, surface maker 1 (*M1S1*), or both [16-21]. It has remained unclear, however, how the phenotype of patients with such a double mutation differs from that of those with the corresponding single mutations. We now describe the first cases of corneal dystrophy associated with both R124H and N544S mutations of *TGFBI*.

METHODS

This study was approved by the ethical review committee for gene analysis research of Yamaguchi University School of Medicine and Yamaguchi University Hospital. After obtaining informed written consent, we extracted genomic DNA from white blood cells of peripheral blood collected from patients in the presence of an anticoagulant. Total RNA

Correspondence to: Naoyuki Yamada, MD, PhD, Department of Ophthalmology, Yamaguchi University Graduate School of Medicine, 1-1-1 Minami Kogushi, Ube City, Yamaguchi, 755-8505, Japan; Phone: +81-836-22-2278; FAX: +81-836-22-2334; email: n.yamada@po.cc.yamaguchi-u.ac.jp

TABLE 1. PCR PRIMERS USED FOR SEQUENCING EXONS OF *TGFBI*.

Exon	Primer	Primer sequence	Annealing temperature (°C)	Product size (bp)
2–9	cDNA-F1	5'-CGCCAAGTCGCCCTACCAG-3'	60	1205
	cDNA-R1	5'-TTGGAGGGGTTCCATCTTTG-3'		
9–17	cDNA-F2	5'-CTCATCCCAGACTCAGCCAA-3'	60	1075
	cDNA-R2	5'-CACATCTCATTATGGTGCGGC-3'		
1	DNA-1F	5'-CCGCTCGCAGCTTACTTAAC-3'	60	362
	DNA-1R	5'-AGCGCTCCAATGCTGCAAGGT-3'		
4	DNA-4F	5'-CGTCCTCTCCACCTGTAGAT-3'	62	350
	DNA-4R	5'-GACTCCCATTCATCATGCCC-3'		
11	DNA-11F	5'-CAGCCTTAATAACCCATCCCA-3'	58	375
	DNA-11R	5'-AATCCCCAAGGTAGAAGAAAG-3'		
12	DNA-12F	5'-AGGAAAATACCTCTCAGCGTGG-3'	60	293
	DNA-12R	5'-ATGTGCCAACTGTTTGCTGC-3'		
13	DNA-13F	5'-GGGAGTTCTTCATTTCAGGG-3'	58	365
	DNA-13R	5'-ATTACACTCAGAGATTCGGG-3'		
14	DNA-14F	5'-GCCTGGGCGACAAGATTGA-3'	58	419
	DNA-14R	5'-CCAACAGCTCCCAATTCAC-3'		

was also extracted from the white blood cells with the use of a QIAmp RNA Blood mini kit (Qiagen, Valencia, CA) and was then subjected to reverse transcription with the use of TaqMan Reverse Transcription Reagents (Applied Biosystems, Foster City, CA). The resulting cDNA as well as genomic DNA were subjected to polymerase chain reaction (PCR) with primers that amplify exons 1, 4, 11, 12, 13, 14, 2–9, or 9–17 of *TGFBI* (Table 1). Each PCR reaction was performed in a total volume of 10 µl containing template DNA (80 ng/µl), 10 pmol of each primer, 200 µM of each deoxynucleoside triphosphate, 20 mM $MgCl_2$, 20 mM Tris-HCl (pH 8.0), 100 mM KCl, and 1 U of Taq polymerase (Ex Taq; Takara, Tokyo, Japan). The reaction mixture was overlaid with 10 µl of mineral oil, and amplification was performed with a Gene Amp PCR System PC808 (ASTEC, Tokyo, Japan) with an initial denaturation at 95 °C for 2 min followed by 30 cycles of denaturation at 94 °C for 30 s, annealing at 58 °C, 60 °C, or 62 °C (Table 1) for 20 s, and extension at 72 °C for 30 s. The PCR products were separated by electrophoresis on a 2% agarose gel and stained with ethidium bromide. For sequencing, 2.5 µl of the PCR products were incubated with 1 µl of ExoSAP-IT (Amersham Bioscience, Tokyo, Japan) first for 20 min at 37 °C and then for another 20 min at 80 °C. Sequencing reactions were then performed with the use of a BigDye Terminator Cycle Sequencing FS Ready Reaction Kit (Applied Biosystems). After purification with ethanol, the reaction products were applied to an ABI 3100-Avant Genetic Analyzer (Applied Biosystems).

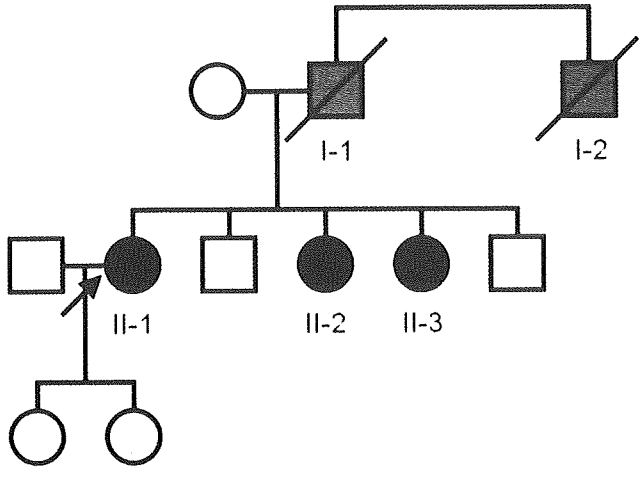

Figure 1. Pedigree of the proband. Black symbols indicate individuals with a diagnosis of corneal dystrophy by genetic analysis. Gray symbols indicate individuals suspected of having been affected by corneal dystrophy but not subjected to genetic analysis. The arrow indicates the proband.

An allele-specific cloning and sequencing approach was applied to characterize the compound heterozygous mutation of R124H and N544S. In brief, cDNA of the proband was subjected to PCR with KOD FX DNA polymerase (Toyobo, Tokyo, Japan) and with the primers, 5′-TGT CCA GCA GCC CTA CCA CTC-3′ (forward) and 5′-AGG ATA TCC CCT CTT TCC TGA GGT C-3′ (reverse; containing an EcoRV restriction site at its 5′ end), to obtain products that included both mutation sites. The PCR products were purified by electrophoresis and digested with EcoRV and BamHI (site in exon 4), and the released fragments were ligated into the multiple cloning site of a sequencing vector (pcDNA3.1[+]; Promega, Madison, WI). The resulting plasmids were expanded in competent *Escherichia coli* JM109 cells (Invitrogen, Carlsbad, CA), and the inserts were then sequenced as described above.

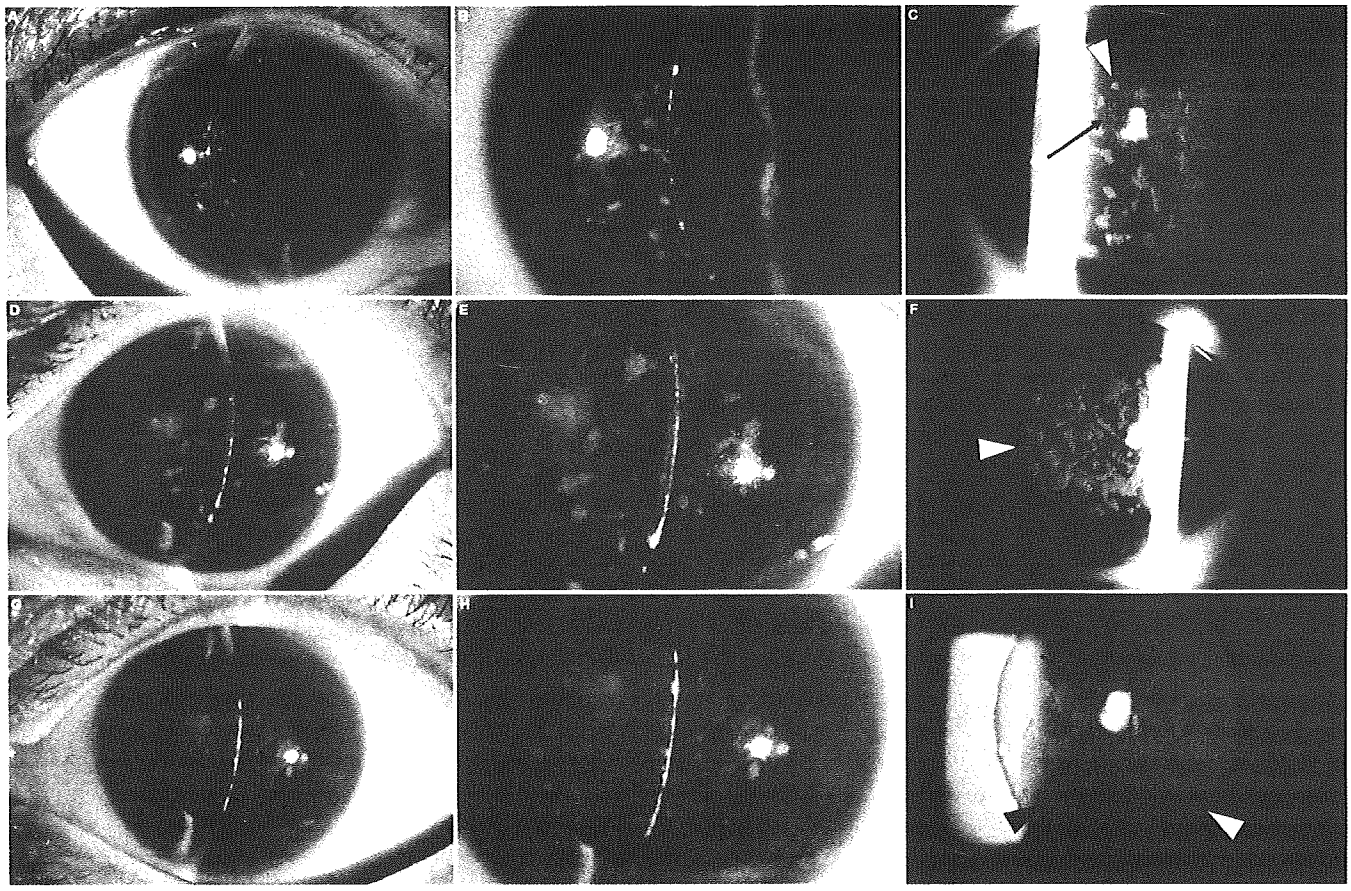

Figure 2. Slit-lamp photographs of the proband and her two sisters. Slit-lamp photographs of the right eye of II-1 (**A–C**), the left eye of II-2 (**D–F**), and the left eye of II-3 (**G–I**) are shown. Granular deposits (gray arrowheads) and star-shaped deposits (black arrowheads) were observed in all three patients (**C**,**F**,**I**) whereas thin lattice lines (black arrows) were observed only in II-1 (**C**) and II-3 (**I**). Nodular deposits were apparent mostly in the superficial-to-middle portion of the corneal stroma in all three patients (**B**,**E**,**H**).

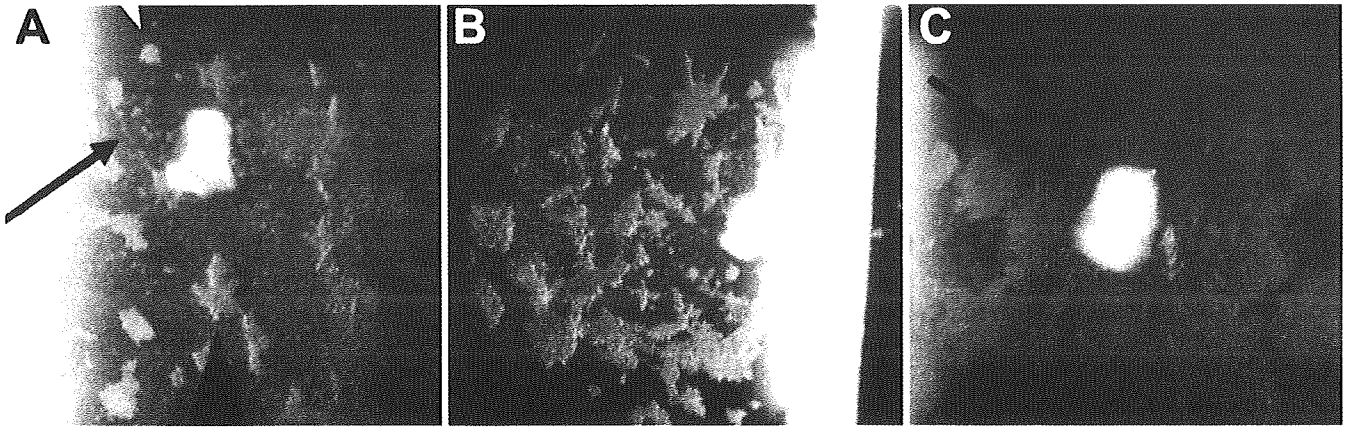

Figure 3. Lattice lines in patient's cornea. The lattice lines referred to in Figure 2 are better visualized in the higher magnifications of Figure 2**C**, Figure 2**F**, and Figure 2**I** (Figure 3**A-C**, respectively). The lattice lines are easily seen in **A** and **C** (black arrows), but not in **B**.

RESULTS

The proband, a 67-year-old Japanese woman (II-1), visited our corneal clinic in January 2000 with a main complaint of gradual impairment of vision (Figure 1). We diagnosed her condition as ACD on the basis of slit-lamp examination. Given that her visual acuity had decreased to 0.7 in the right eye and 0.4 in the left eye, we performed phototherapeutic keratectomy on her left eye in March 2000 and on her right eye in May 2000. The parents of II-1 were not related to each other. Her father (I-1) is no longer alive, and she has two

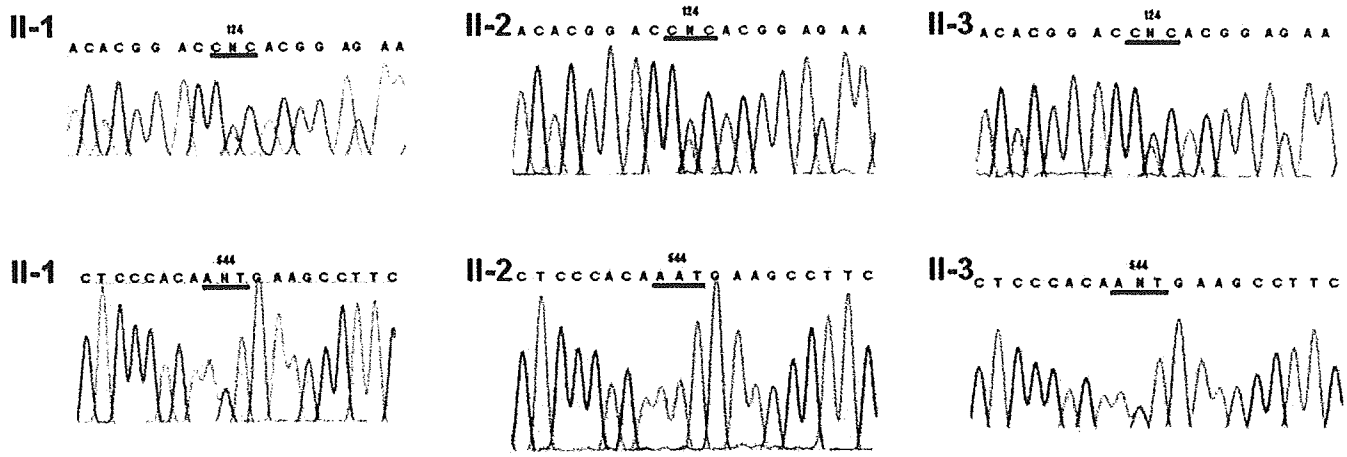

Figure 4. Genetic analysis of *TGFBI* in the proband and her two sisters. Direct sequencing of genomic amplification products corresponding to exon 4 (upper panels) or exon 12 (lower panels) of *TGFBI* was performed for II-1, II-2, and II-3. A heterozygous CGC→CAC mutation was detected at codon 124 in II-1, II-2, and II-3. A heterozygous AAT→AGT mutation was detected at codon 544 in II-1 and II-3.

brothers and two sisters. Her father's brother (I-2) and her sisters (II-2, II-3) were also diagnosed at our clinic with ACD by slit-lamp examination. Her reporting suggested that her father (I-1) had corneal dystrophy. We also performed phototherapeutic keratectomy on the left eye of II-2 in March 2000 and on the right eye of II-2 in May 2000.

Slit-lamp examination subsequently revealed multiple granular regions of opacity in the surface-to-middle portion of the corneal stroma in both eyes of II-1, II-2, and II-3. Lattice lines were also observed in II-1 (Figure 2A–C) and II-3 (Figure 2G–I) but not in II-2 (Figure 2D–F). These lattice lines can be seen better in the higher magnifications of Figure 2C, Figure 2F and Figure 2I (Figure 3A-C, respectively). Both II-1 and II-3 were found to harbor both a heterozygous CGC→CAC (Arg→His) mutation at codon 124 and a heterozygous AAT→AGT (Asn→Ser) mutation at codon 544 of *TGFBI* whereas II-2 harbored only the heterozygous CGC→CAC (Arg→His) mutation at codon 124 (Figure 4). The mutations were identified at both the genomic and cDNA levels.

To investigate whether the two *TGFBI* mutations are on the same or different chromosomes of the proband, we adopted an allele-specific cloning and sequencing approach. PCR products containing both mutation sites were subcloned and sequenced. Of three independent clones analyzed, one contained only the R124H mutation and the other two contained only the N544S mutation, indicating that the two mutations are on different chromosomes.

DISCUSSION

As far as we are aware, this is the first report of a patient with a double mutation of *TGFBI* causing an autosomal dominant form of corneal dystrophy. The clinical manifestations of the two cases with both R124H and N544S mutations appeared to be a summation of those of Avellino and lattice corneal dystrophies. We observed lattice lines in the corneas of II-1 and II-3, both of whom have the N544S mutation of *TGFBI*, but not in II-2, who harbors only the R124H mutation.

We were not able to perform genetic analysis on I-1 and I-2 because they were no longer alive at the time of this analysis. However, allele-specific cloning and sequencing revealed that the R124H and N544S mutations are on different chromosomes, consistent with our clinical findings. Slit-lamp examination of I-2 did not reveal the presence of lattice lines, suggesting that the R124H mutation was transmitted to the proband and her two sisters from I-1. Although slit-lamp examination was not performed on the mother of the three sisters because of her being confined to bed, it is likely that she harbors the N544S mutation of *TGFBI*. Given that the clinical manifestation of the N544S mutation has a late onset and that the mutation does not have a pronounced effect on visual acuity, the mother may not experience a visual disturbance.

Several cases of double mutations associated with corneal dystrophies other than macular corneal dystrophy have been described previously (Table 2). However, no case of a double mutation of *TGFBI* causing an autosomal dominant form of corneal dystrophy has previously been reported. The presence of a homozygous Q118X mutation of *MISI* and a heterozygous P501T mutation of *TGFBI* in the same individual was described [16]. The Q118X mutation of *MISI* causes gelatinous drop-like corneal dystrophy (GDLD) with an autosomal recessive mode of inheritance. The P501T mutation of *TGFBI* causes LCD type IIIA [6]. The clinical manifestation in this patient resembled that of GDLD but not that of LCD type IIIA. A patient with a clinical diagnosis of GDLD and heterozygous Q118X and Y184C mutations of *MISI* has also been described [17]. No other case of the Y184C mutation in *MISI* has been presented, so it is not clear whether this mutation in the homozygous state can cause GDLD. A patient with a clinical diagnosis of GDLD was found to be heterozygous for both Q118X and L186P

TABLE 2. PREVIOUS REPORTS OF DOUBLE MUTATIONS ASSOCIATED WITH CORNEAL DYSTROPHY.

Case	Amino acid mutation	Hetero- or homozygote	Gene	Mode of inheritance	Phenotype of single mutation	Phenotype of double mutation	Reference
1	Q118X	Homozygote	*M1S1*	AR	GDLD	GDLD	[16]
	P501T	Heterozygote	*TGFBI*	AD	LCD		
2	Q118X	Heterozygote	*M1S1*	AR	GDLD	GDLD	[17]
	Y184C	Heterozygote	*M1S1*	Not identified	Not identified		
3	Q118X	Heterozygote	*M1S1*	AR	GDLD	GDLD	[18]
	L186P	Heterozygote	*M1S1*	AR	GDLD		
4	A546D	Heterozygote	*TGFBI*	AD	Polymorphic corneal amyloidosis or LCD	LCD	[19,20]
	P551Q	Heterozygote	*TGFBI*	Not identified	Not identified		
5	R124L	Heterozygote	*TGFBI*	AD	GCD	GCD	[21]
	DeltaT125-DeltaE126	Heterozygote	*TGFBI*	Not identified	Not identified		
Present case	R124H	Heterozygote	*TGFBI*	AD	ACD	ACD+LCD	Present study
	N544S	Heterozygote	*TGFBI*	AD	LCD		

Abbreviations: ACD, Avellino corneal dystrophy; AD, autosomal dominant; AR, autosomal recessive; GCD, granular corneal dystrophy; GDLD, gelatinous droplike corneal dystrophy; LCD, lattice corneal dystrophy.

mutations of *M1S1* [18]. Patients with a clinical diagnosis of atypical LCD were found to be heterozygous for both A546D and P551Q mutations of *TGFBI* [19,20]. The A546D mutation of *TGFBI* causes polymorphic corneal amyloidosis [22] or atypical LCD [23] with an autosomal dominant mode of inheritance. There have been no other reports of the P551Q mutation of *TGFBI*, so it is not clear whether a heterozygous P551Q mutation causes corneal dystrophy. Finally, a patient with a clinical diagnosis of granular corneal dystrophy was found to be heterozygous for both R124L and ΔT125-ΔE126 mutations of *TGFBI* [21]. There have been no other reports of the ΔT125-ΔE126 mutation of *TGFBI*.

A few studies have addressed the penetrance of inherited corneal dystrophy. LCD type IIIA caused by the P501T mutation of *TGFBI* [16] and atypical granular corneal dystrophy caused by the D123H mutation of *TGFBI* [24] are thought to have a low penetrance. Non-penetrance of ACD has also been described [25]. The penetrance of corneal dystrophies caused by the R124H or N544S mutations of *TGFBI* remains unclear.

In all previously reported cases of double mutations, the clinical phenotype resembled that of one but not both of the associated corneal dystrophies. In the cases described in the present study, the phenotype associated with the double mutation is the summation of both corneal dystrophies. These cases thus indicate that R124H and N544S mutations of *TGFBI* independently determine clinical manifestation.

REFERENCES

1. Skonier J, Neubauer M, Madisen L, Bennett K, Plowman GD, Purchio AF. cDNA cloning and sequence analysis of beta ig-h3, a novel gene induced in a human adenocarcinoma cell line after treatment with transforming growth factor-beta. DNA Cell Biol 1992; 11:511-22. [PMID: 1388724]
2. Munier FL, Korvatska E, Djemai A, Le Paslier D, Zografos L, Pescia G, Schorderet DF. Kerato-epithelin mutations in four 5q31-linked corneal dystrophies. Nat Genet 1997; 15:247-51. [PMID: 9054935]
3. Munier FL, Frueh BE, Othenin-Girard P, Uffer S, Cousin P, Wang MX, Heon E, Black GC, Blasi MA, Balestrazzi E, Lorenz B, Escoto R, Barraquer R, Hoeltzenbein M, Gloor B, Fossarello M, Singh AD, Arsenijevic Y, Zografos L, Schorderet DF. BIGH3 mutation spectrum in corneal dystrophies. Invest Ophthalmol Vis Sci 2002; 43:949-54. [PMID: 11923233]
4. Kannabiran C, Klintworth GK. TGFBI gene mutations in corneal dystrophies. Hum Mutat 2006; 27:615-25. [PMID: 16683255]
5. Endo S, Nguyen TH, Fujiki K, Hotta Y, Nakayasu K, Yamaguchi T, Ishida N, Kanai A. Leu518Pro mutation of the beta ig-h3 gene causes lattice corneal dystrophy type I. Am J Ophthalmol 1999; 128:104-6. [PMID: 10482106]
6. Yamamoto S, Okada M, Tsujikawa M, Shimomura Y, Nishida K, Inoue Y, Watanabe H, Maeda N, Kurahashi H, Kinoshita S, Nakamura Y, Tano Y. A kerato-epithelin (betaig-h3) mutation in lattice corneal dystrophy type IIIA. Am J Hum Genet 1998; 62:719-22. [PMID: 9497262]
7. Fujiki K, Hotta Y, Nakayasu K, Yokoyama T, Takano T, Yamaguchi T, Kanai A. A new L527R mutation of the betaIGH3 gene in patients with lattice corneal dystrophy with deep stromal opacities. Hum Genet 1998; 103:286-9. [PMID: 9799082]
8. Mashima Y, Yamamoto S, Inoue Y, Yamada M, Konishi M, Watanabe H, Maeda N, Shimomura Y, Kinoshita S. Association of autosomal dominantly inherited corneal dystrophies with BIGH3 gene mutations in Japan. Am J Ophthalmol 2000; 130:516-7. [PMID: 11024425]
9. Dighiero P, Drunat S, Ellies P, D'Hermies F, Savoldelli M, Legeais JM, Renard G, Delpech M, Grateau G, Valleix S. A new mutation (A546T) of the betaig-h3 gene responsible for a French lattice corneal dystrophy type IIIA. Am J Ophthalmol 2000; 129:248-51. [PMID: 10682981]
10. Kawashima M, Yamada M, Funayama T, Mashima Y. Six cases of late-onset lattice corneal dystrophy associated with gene mutations induced by the transforming growth factor-beta.

Nippon Ganka Gakkai Zasshi 2005; 109:93-100. [PMID: 15770959]

11. Mashima Y, Konishi M, Nakamura Y, Imamura Y, Yamada M, Ogata T, Kudoh J, Shimizu N. Severe form of juvenile corneal stromal dystrophy with homozygous R124H mutation in the keratoepithelin gene in five Japanese patients. Br J Ophthalmol 1998; 82:1280-4. [PMID: 9924333]
12. Okada M, Yamamoto S, Watanabe H, Inoue Y, Tsujikawa M, Maeda N, Shimomura Y, Nishida K, Kinoshita S, Tano Y. Granular corneal dystrophy with homozygous mutations in the kerato-epithelin gene. Am J Ophthalmol 1998; 126:169-76. [PMID: 9727509]
13. Okada M, Yamamoto S, Inoue Y, Watanabe H, Maeda N, Shimomura Y, Ishii Y, Tano Y. Severe corneal dystrophy phenotype caused by homozygous R124H keratoepithelin mutations. Invest Ophthalmol Vis Sci 1998; 39:1947-53. [PMID: 9727418]
14. Fujiki K, Hotta Y, Nakayasu K, Kanai A. Homozygotic patient with betaig-h3 gene mutation in granular dystrophy. Cornea 1998; 17:288-92. [PMID: 9603385]
15. Inoue T, Watanabe H, Yamamoto S, Inoue Y, Okada M, Hori Y, Maeda N, Hayashi K, Shimomura Y, Tano Y. Different recurrence patterns after phototherapeutic keratectomy in the corneal dystrophy resulting from homozygous and heterozygous R124H BIG-H3 mutation. Am J Ophthalmol 2001; 132:255-7. [PMID: 11476689]
16. Ha NT, Fujiki K, Hotta Y, Nakayasu K, Kanai A. Q118X mutation of M1S1 gene caused gelatinous drop-like corneal dystrophy: the P501T of BIGH3 gene found in a family with gelatinous drop-like corneal dystrophy. Am J Ophthalmol 2000; 130:119-20. [PMID: 11004271]
17. Tian X, Fujiki K, Li Q, Murakami A, Xie P, Kanai A, Wang W, Liu Z. Compound heterozygous mutations of M1S1 gene in gelatinous droplike corneal dystrophy. Am J Ophthalmol 2004; 137:567-9. [PMID: 15013888]
18. Taniguchi Y, Tsujikawa M, Hibino S, Tsujikawa K, Tanaka T, Kiridoushi A, Tano Y. A novel missense mutation in a Japanese patient with gelatinous droplike corneal dystrophy. Am J Ophthalmol 2005; 139:186-8. [PMID: 15652848]
19. Klintworth GK, Bao W, Afshari NA. Two mutations in the TGFBI (BIGH3) gene associated with lattice corneal dystrophy in an extensively studied family. Invest Ophthalmol Vis Sci 2004; 45:1382-8. [PMID: 15111592]
20. Aldave AJ, Gutmark JG, Yellore VS, Affeldt JA, Meallet MA, Udar N, Rao NA, Small KW, Klintworth GK. Lattice corneal dystrophy associated with the Ala546Asp and Pro551Gln missense changes in the TGFBI gene. Am J Ophthalmol 2004; 138:772-81. [PMID: 15531312]
21. Dighiero P, Drunat S, D'Hermies F, Renard G, Delpech M, Valleix S. A novel variant of granular corneal dystrophy caused by association of 2 mutations in the TGFBI gene-R124L and DeltaT125-DeltaE126. Arch Ophthalmol 2000; 118:814-8. [PMID: 10865320]
22. Eifrig DE Jr, Afshari NA. Buchanan HWt, Bowling BL, Klintworth GK. Polymorphic corneal amyloidosis: a disorder due to a novel mutation in the transforming growth factor beta-induced (BIGH3) gene. Ophthalmology 2004; 111:1108-14. [PMID: 15177960]
23. Correa-Gomez V, Villalvazo-Cordero L, Zenteno JC. The TGFBI A546D mutation causes an atypical type of lattice corneal dystrophy. Mol Vis 2007; 13:1695-700. [PMID: 17893671]
24. Ha NT. Cung le X, Chau HM, Thanh TK, Fujiki K, Murakami A, Kanai A. A novel mutation of the TGFBI gene found in a Vietnamese family with atypical granular corneal dystrophy. Jpn J Ophthalmol 2003; 47:246-8. [PMID: 12782158]
25. Kim JW, Kim HM, Song JS. Phenotypic non-penetrance in granular corneal dystrophy type II. Graefes Arch Clin Exp Ophthalmol 2008; 246:1629-31. [PMID: 18458933]

The print version of this article was created on 11 May 2009. This reflects all typographical corrections and errata to the article through that date. Details of any changes may be found in the online version of the article.

Biochemical and Biophysical Research Communications 379 (2009) 547–552

Contents lists available at ScienceDirect

Biochemical and Biophysical Research Communications

journal homepage: www.elsevier.com/locate/ybbrc

Obesity causes a shift in metabolic flow of gangliosides in adipose tissues

Aya Tanabe [a], Morihiro Matsuda [a], Atsunori Fukuhara [a], Yugo Miyata [a], Ryutaro Komuro [a], Iichiro Shimomura [a], Hiromasa Tojo [b,*]

[a] Department of Metabolic Medicine, Osaka University Graduate School of Medicine, 2-2 Yamadaoka, Suita, Osaka 565-0871, Japan
[b] Department of Biophysics and Biochemistry, Osaka University Graduate School of Medicine, 2-2 Yamadaoka, Suita, Osaka 565-0871, Japan

ARTICLE INFO

Article history:
Received 10 December 2008
Available online 29 December 2008

Keywords:
Ganglioside
Adipose tissue
Macrophage

ABSTRACT

Obesity is associated with insulin resistance and a mild chronic inflammation in adipose tissues. Recent studies suggested that GM3 ganglioside mediates dysfunction in insulin signaling. However, it has not been determined the ganglioside profiling in adipose tissues of obese animals. Here, we for the first time examined semi-quantitative ganglioside profiles in the adipose tissues of high fat- and high sucrose-induced obese, diabetic C57BL/6J mice by TLC and HPLC/mass spectrometry. In control adipose tissues GM3 dominated with traces of GM1 and GD1a; obesity led to a dramatic increase in GM2, GM1, and GD1a with the GM3 content unchanged. Similar results were obtained in KK and KKAy mice. Adipocytes separated from stromal vascular cells including macrophages contained more of those gangliosides in KKAy mice than in KK mice. These results underscore those gangliosides in the pathophysiology of obesity-related diseases.

Obesity is a state of chronic inflammation of adipose tissue and recent studies indicated that adipose tissue macrophages are strongly associated with obesity-induced complications in both rodents and humans [1]. The number of F4/80-positive macrophages in adipose tissues significantly correlated with both adipocyte size and body mass [2]. Adipose tissue macrophages produce significant amounts of proinflammatory cytokines, such as TNFα and IL-6 [2], and pharmacological inhibition of macrophage migration lowered the macrophage content of adipose tissue with improved insulin sensitivity [3]. Consequently, adipose tissue macrophages play a significant role in the pathology of obesity.

Gangliosides belong to one of the major glycosphingolipids in mammals, concentrated in lipid microdomains, and contain different numbers of sialyl residue in the defined sugar sequence. Sialylation of lactosylceramide leads to monosialoganglioside GM3, which is then converted sequentially into a-series gangliosides by the actions of specific glycosyltransferases [4]. Gangliosides are known to play major roles as mediators for cell–cell or cell–matrix recognition, and act as modulators of transmembrane signal transducers, and of regulating cell proliferation [5]. Moreover, gangliosides are implicated in insulin resistance. GM3 synthase-deficient mice showed increased insulin sensitivity with enhanced insulin receptor phosphorylation in skeletal muscle, and were less prone to high fat diet-induced insulin resistance [6]. In 3T3-L1 adipocytes treatment with GM3 suppressed insulin-induced phosphorylation of insulin receptor and IRS-1 [7], and reducing gangliosides content by a glucosylceramide synthase inhibitor PDMP improved TNFα-induced insulin resistance [7].

These studies suggest that ganglioside contents in adipose or other tissues are associated with insulin signaling mechanisms. However, detailed ganglioside profiles in obese adipose tissues of both disease model, animals and man have not yet been determined. Here, we for the first time demonstrate that a-series gangliosides GM2, GM1, and GD1a are dramatically increased in the adipose tissues of obese mice by normal-phase HPLC/mass spectrometry (HPLC/MS).

Materials and methods

Reagent. For lipid analysis, DEAE–Sephadex A-25 was purchased from GE Healthcare (Waukesha, WI), and Sep-pack C18 cartridge column from Waters (Tokyo, Japan) and Silica gel 60 high-performance thin-layer chromatography plates (HPTLC) from Merck (Darmstadt, FRG). Highly purified gangliosides (GM3, GM2, GM1, GD1a, GD1b, and GT1b) were purchased from Matreya (Pleasant Gap, PA) and stored at −20 °C.

Animals. Male C57BL/6J mice, and female KKAy and KK mice were purchased from CLEA Japan. Male C57BL/6J mice were fed high fat/high sucrose (HF/HS) diet for 35 weeks. HF/HS diet: 14% beef tallow, 14% lard, 2% soybean oil, 20% sucrose, 25% milk casein, 15% corn starch, 5% cellulose, 3.5% mineral mixture, and 1% vitamin mixture. Perigonadal white adipose tissue (WAT) and epididymal WAT were dissected and immediately frozen in liquid nitrogen.

* Corresponding author. Fax: +81 6 6879 3742.
E-mail address: htojo@mr-mbio.med.osaka-u.ac.jp (H. Tojo).

0006-291X/$ - see front matter © 2008 Elsevier Inc. All rights reserved.
doi:10.1016/j.bbrc.2008.12.086

Fractioning of adipose tissues. Epididymal fat pads from female KK and KKAy mice were excised and minced in Krebs-Ringer-bicarbonate-HEPES (N-2-hydroxyethylpiperazine-N′-ethanesulfonic acid) buffer which contained 120 mM NaCl, 4 mM KH_2PO_4, 1 mM $MgSO_4$, 1 mM $CaCl_2$, 10 mM $NaHCO_3$, 30 mM HEPES, 20 μM adenosine, and 4% (w/v) bovine serum albumin (Calbiochem, San Diego, CA). Tissue suspensions were centrifuged at 500*g* for 5 min to remove erythrocytes and free leukocytes. Collagenase was added to the final concentration of 2 mg/ml and incubated at 37 °C for 20 min with shaking. The cell suspension was filtered through a 250-μm filter and then spun at 300*g* for 1 min to separate floating mature adipocytes fraction (MA) from the stromal vascular fraction (SV) pellet. This fractioning and washing procedure were repeated twice with Krebs-Ringer-bicarbonate-HEPES buffer. Finally both fractions were washed with phosphate buffered saline.

Isolation and analysis of gangliosides. Gangliosides were isolated from epididymal and perigonadal WAT and cell fractions by the procedure of Pacuszka [8] with some modifications. Four hundred milligrams of epididymal WAT was extracted twice with 4 ml of chloroform:methanol (2:1, v/v) under sonitation in a bath for 20 min, and the residues were re-extracted sequentially with 4 ml of chloroform:methanol (1:1, v/v) twice, chloroform:methanol (1:2) twice, and chloroform:methanol:distilled water (4:8:3, v/v/v) twice. The combined extracts were dried under nitrogen flow, dissolved in 1 ml of chloroform:methanol (2:1, v/v) and applied to a DEAE–Sephadex A-25 column (1.5 × 8 cm; acetate form). The column was washed with 24 ml of chloroform:methanol: water (30:60:8, v/v/v) and then chloroform:methanol:water (60:35:8, v/v/v) to remove neutral lipids. Then, acidic lipids including gangliosides were eluted with 24 ml of methanol containing 200 mM ammonium acetate. The solvent was dried under nitrogen, and the residue was dissolved in 2 ml of 0.5 M NaOH in methanol, refluxed at 65 °C for 2 h to saponify ester-containing lipids including phospholipids. The mixture was neutralized with 1 M acetic acid solution, diluted with water, and applied on a Sep-Pack C18 cartridge column, which was pre-equilibrated with 50% methanol/water. The column was washed with 32 ml of methanol:water (1:1, v/v). Then gangliosides were eluted with 24 ml of methanol. The isolated gangliosides were separated by HPTLC with chloroform:methanol: 0.25% $CaCl_2$ (60:35:8, v/v/v) as the developing solvent, and visualized with orcinol in 10% H_2SO_4 at 105 °C for 10 min.

RNA isolation and quantitative real-time RT-PCR. Total RNA was extracted from cells and tissues using RNA STAT-60 Reagent (Tel-Test, Friendswood, TX) or Sepasol (Nacalai Tesque, Kyoto, Japan), according to the manufacturer's instructions. One microgram of total RNA was converted to cDNA using Transcriptor First Strand cDNA Synthesis Kit (Roche Diagnostics, Mannheim, Germany). Quantitative real-time RT-PCR was performed on Light Cycler Real-Time PCR instrument (Roche) using SYBR Green (Roche) in a 20-μl reaction mixture. The sequences of primers are listed in the Supplementary Table. The relative amount of mRNA was calculated from an internal standard curve, and normalized to expression levels of cyclophilin.

Ganglioside analysis by HPLC/mass spectrometry. One of the authors (HT) has developed a method capable of analyzing a wider range of lipid classes from neutral lipids to phospholipids on a single normal-phase chromatographic run with three solvent (A–C) gradients and post-column mixing of solvent D that helps electrospray ionization (ESI) of lipids eluted earlier with non-polar solvents. The present method is based on the phospholipid analysis mode [9,10] of the comprehensive method, which uses a binary gradient (solvents B–C) without ESI-assisting solvent D. To separate gangliosides being more polar than phospholipids on microbore normal-phase HPLC, the water contents in solvent C was increased according to the methods of Kundu and Scott [11] and the final concentration of 20 mM ammonium formate was added to it for improving chromatographic resolution and ESI efficiency. Lipid extracts containing gangliosides were prepared as described above, and an aliquot was supplemented with appropriate amounts (usually 5 pmol) of bovine brain GT1b as internal standard, which is not contained in murine adipose gangliosides. For the measurements of fractioned samples, 500 pmol of GT1b was added to cell fractions prior to extraction. The GT1b consists mainly of C20:0 (70%) and C18:0 (30%) species with an average monoisotopic molecular weight of 2146.7. An aliquot (2–2.5 μl) of the mixtures was directly subjected to HPLC/mass spectrometry.

Statistical analysis. All data were expressed as means ± SEM. Differences between groups were examined for statistical significance using the unpaired Student's *t*-test. A *p* value less than 0.05 denoted the presence of a statistically significant difference.

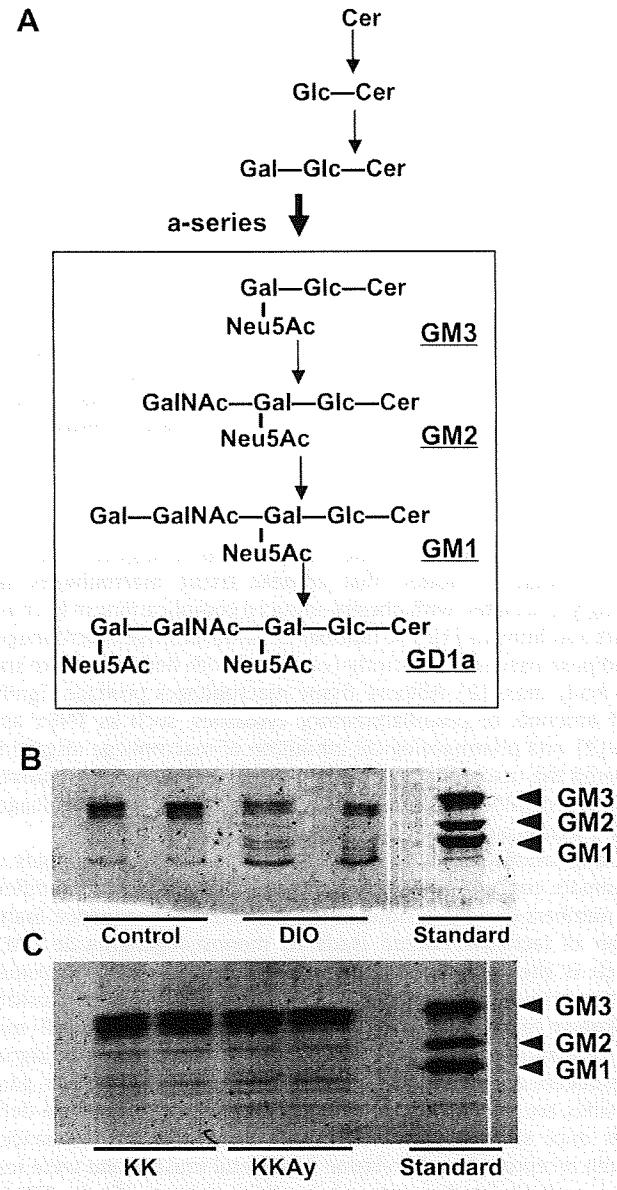

Fig. 1. TLC profiles of gangliosides of control and obese adipose tissues. (A) Structures and de novo metabolic pathway of a-series gangliosides. Cer, ceramide; Glc, glucose; Gal, galactose; GalNac, N-acetylgalactosamine; Neu5AC, N-acetylneuramic acid. (B) Gangliosides isolated from control and DIO epididymal adipose tissues were separated on TLC using the solvent system as described in H_2SO_4, and TLC plates were visualized with the orcinol-Materials and methods reagent. On the standard lane, an aliquot of standard GM3, GM2, and GM1 mixtures was developed ($n = 2$ each). (C) Gangliosides isolated from KK and KKAy perigonadal adipose tissue were separated on TLC as in B ($n = 2$ each).

Results

A synopsis of the severity of obesity and type 2 diabetes in model mice

In this study, we used mice with diet-induced obesity (DIO) generated by long-term feeding of HS/HF diet for 35 weeks as a mimic for human lifestyle-induced obesity with reference to genetic obesity models, 10-week-old KK mice and its congenic and more obese strain KKAy with the lethal yellow (agouti) gene. To check the severity of obesity and type 2 diabetes, body weight and plasma glucose levels were examined in each animal group. Body weights and plasma glucose levels of DIO mice (51.8 ± 3.1 g, and 239 ± 6.8 mg/dl, respectively) indeed showed they were obese and diabetic, compared with those of controls (37.2 ± 1.2 g, $p < 0.05$ and 174 ± 9.5 mg/dl, $p < 0.01$, respectively). The same data pairs show that KKAy mice (44.4 ± 1.1 g, and 435 ± 44 mg/dl, respectively) were more obese and diabetic than KK mice (35.4 ± 1.0 g, $p < 0.001$, and 256 ± 8 mg/dl, $p < 0.05$, respectively).

Effects of HF/HS DIO on ganglioside profiles in adipose tissues

To explore the functional roles of gangliosides residing preferentially in lipid microdomains in obesity pathophysiology, we first examined detailed ganglioside profiles in control and DIO epididymal adipose tissues by TLC and HPLC/MS as described in Materials and methods. The structures of a-series gangliosides relevant to this study and their metabolic pathway are shown in Fig. 1A. Extensive solvent extraction, and treatments on an anion-exchange and a reverse-phase column as described in Materials and methods were required for successful analysis, because of huge amounts of triacylglycerols in the adipose tissues. TLC separated adipose gangliosides into the faster migrating major band (the R_f value of 0.48) corresponding to a GM3 standard and trace bands in its behind in control mice; DIO led to a significant decrease in the GM3 band intensity on the tissue weight basis and in turn a marked increase in the intensity of the slowest band (the R_f value of 0.33) corresponding to a ganglioside class with more sugar than GM1, possibly GD1 (Fig. 1B).

Next we compared the amounts of gangliosides in each animal group by HPLC/MS using GT1b as internal standard, because endogenous GT1b was undetectable in any adipose tissue samples examined. Hereafter, ganglioside levels are reported as the ratio of the peak area of a molecular species assigned by HPLC/MS to that of internal standard GT1b, and normalized to protein concentration. In control mice GM3 dominated and only trace of GD1a were detectable, while the adipose tissues of DIO mice contain considerable amounts of a-series gangliosides including GM2, GM1, and GD1a as well as GM3 (Fig. 2A), consistent with the results of TLC. The GM3 levels normalized to the protein concentration were unchanged (Fig. 2A), because the protein concentrations per tissue

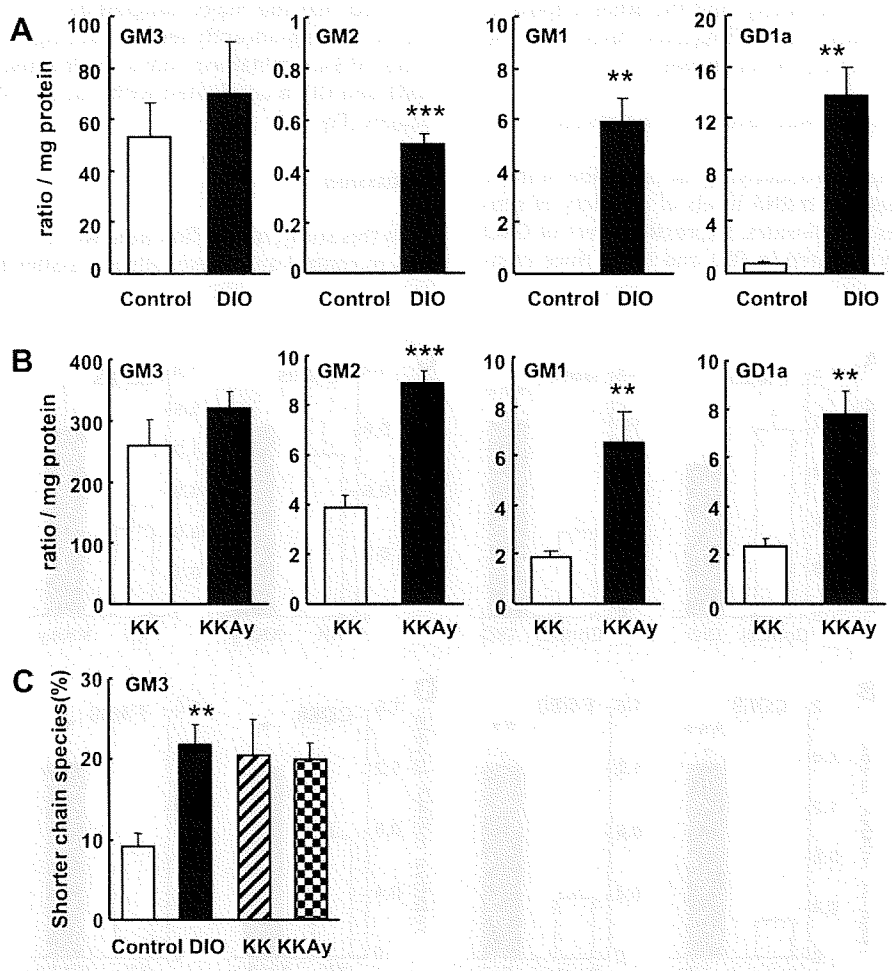

Fig. 2. Ganglioside profiling by HPLC/MS in control and obese adipose tissue. (A) The total levels of GM3, GM2, GM1, and GD1a isolated from control and DIO epididymal adipose tissues. The values were reported as the sum of quantitatively significant peak areas corresponding to molecular species assigned by HPLC/MS, and normalized to the peak area of internal standard GT1b and protein concentration. (B) The total levels of GM3, GM2, GM1, and GD1a isolated from KK and KKAy perigonadal adipose tissue as in (A). (C) The proportion of shorter chain species (16:0 and 18:0) of GM3 in control, DIO, KK and KKAy mice. $^{**}p < 0.01$, compared with control mice ($n = 4$ each).

weight of the DIO adipose tissues were about a half of those of control. In addition, GM3 in the DIO tissues contained a significantly increased proportion of palmitoyl (16:0) and stearoyl (18:0) species (Fig. 2C). On-line data-dependent tandem MS showed that GM3 mainly comprised molecular species with mono-hydroxylated fatty acyl and N-acetylneuraminyl moieties, and the other adipose a-series gangliosides those with non-hydroxylated fatty acyl and N-glycolylneuraminyl moieties (data not shown).

Ganglioside profiling in adipose tissues of KK and KKAy mice

To compare the adipose ganglioside profiles in DIO with those in genetic obesity, we determined a-series gangliosides from perigonadal adipose tissue of KK and KKAy mice (Figs. 1C and 2B). TLC separated adipose gangliosides into the faster migrating major band (the R_f value of 0.51) corresponding to a GM3 standard and trace bands in its behind in KK and KKAy mice. There were no differences in GM3 amounts on the tissue weight basis between KK and KKAy mice (Fig. 1C). In accordance with these results, the GM3 levels per mg protein were not significantly different between KK and KKAy mice (Fig. 2B), but ~4-fold greater than those of the former model (Fig. 2A). Like the diet-induced model, a-series gangliosides more complex than GM3 were markedly enriched in the genetic models (Fig. 2B), and the levels of GM3 species containing 16:0 and 18:0 did not change between KK and KKAy mice (Fig. 2C). In the genetic models, GM3 mainly comprised molecular species with either N-acetylneuraminyl or N-glycolylneuraminyl moiety, and non-hydroxylated fatty acyl moiety, and the other adipose a-series gangliosides those with non-hydroxylated fatty acyl and N-glycolylneuraminyl moieties (data not shown).

mRNA expression of GM2 synthase was elevated in DIO and KKAy mice

To investigate the mechanism underlying the induction of these gangliosides, we next measured mRNA levels of a variety of synthases relevant to a-series gangliosides. Expression level of GM2 synthase was significantly elevated in DIO and KKAy mice compared with each control group, whereas expressions of GM3, GM1, and GD1a synthases were not (Fig. 3A, C, and Supplementary Figure).

Contribution of adipocytes and infiltrated macrophage to ganglioside profiles

In obese mice, macrophages infiltrate into adipose tissues, and are the major source of inflammatory cytokines [2]. In accordance with previous reports, the expression levels of macrophage markers CD68 and F4/80 were markedly increased in DIO mice compared to control mice (Fig. 3B). Similar results were observed in the genetic models (Fig. 3D). This suggests that macrophage infiltration could be involved in adipose ganglioside profiles altered in obesity. To check this, stromal vascular cell (SV) fractions containing macrophages were separated from mature adipocytes (MA) fractions with the adipose tissues of KK and KKAy mice. In both fractions, the levels of GM2, GM1, and GD1a correlated with degree of obesity (Fig. 4B). The changes in those levels between KK and KKAy mice were more drastic in MA fraction than in the SV fraction (Fig. 4B). The GM3 level of KK mice was comparable with that of KKAy mice in MA fraction, while that in the SV fraction from KKAy mice tended to decrease, compared to that from KK mice (Fig. 4A).

To further examine cell type-specific ganglioside profiles, lipid extracts were obtained from 3T3-L1 pre-adipocytes, differentiated 3T3-L1 adipocytes and macrophage cell line RAW264. TLC analysis revealed that the major ganglioside of 3T3-L1 was GM3, and its levels were significantly reduced during differentiation into adipocytes. 3T3-L1 contained only a small amount of GD1a. In contrast, GM1 and GD1a dominated with trace of GM3 in RAW264 macrophages (Fig. 4C).

Discussion

In this study, for the first time we dissected the ganglioside profiles in control and obese adipose tissues by normal-phase HPLC/

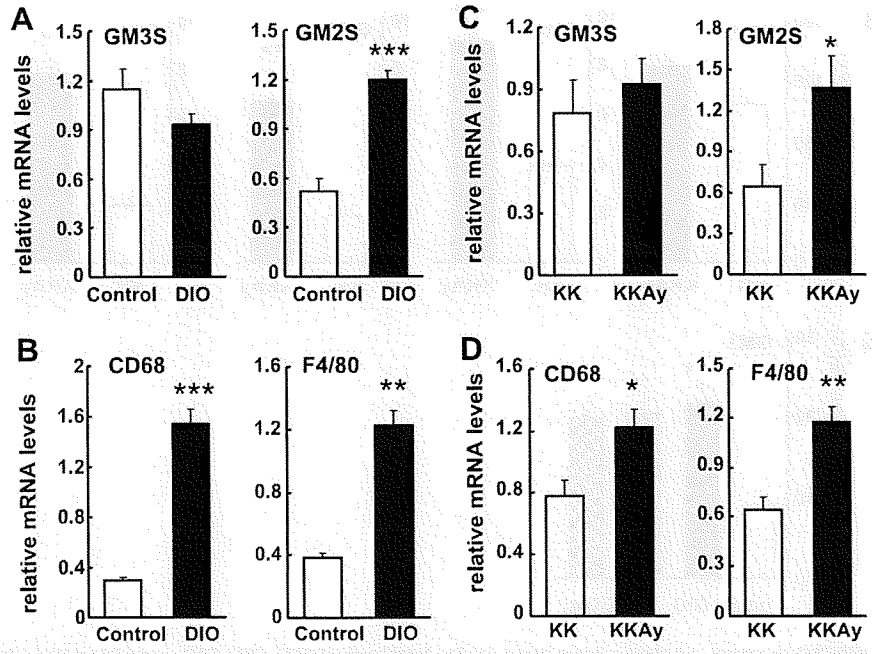

Fig. 3. Expression levels of genes for ganglioside (GM2 and GM3) synthases and macrophage markers CD68 and F4/80 in adipose tissues of control and obese mice. mRNA expressions of indicated genes were measured by quantitative RT-PCR. Values were normalized to the level of cyclophilin mRNA and expressed as means ± SEM ($n = 4$). $^{*}p < 0.05$, $^{**}p < 0.01$, $^{***}p < 0.001$; (A,B) control vs. DIO. (C,D) KK vs. KKAy.

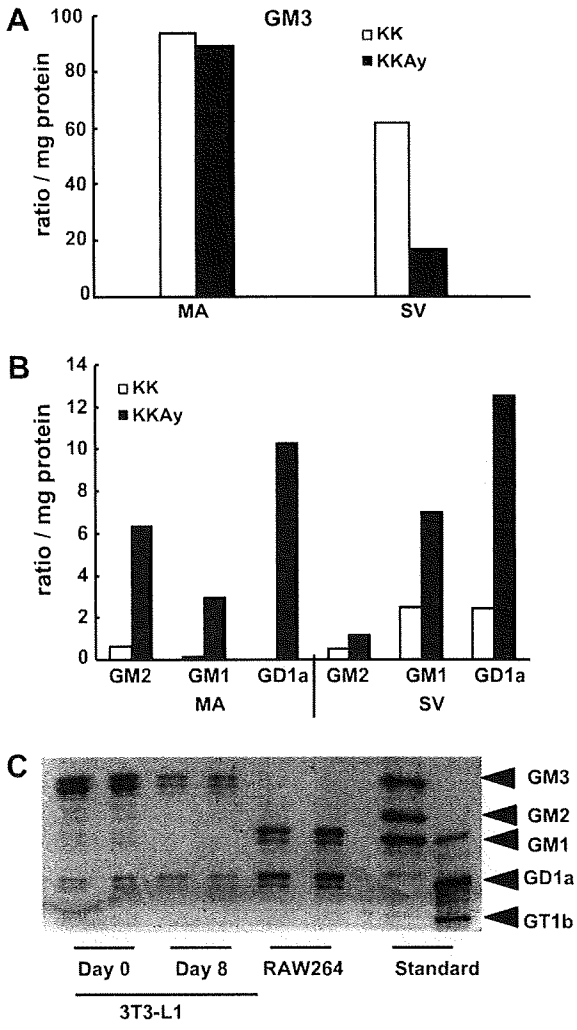

Fig. 4. Ganglioside profiles in cell fractions isolated from adipose tissues. (A,B) Perigonadal adipose tissue of KK and KKAy mice (pooled samples from four mice) were fractionated into stromal vascular cell (SV) fractions and mature adipocyte (MA) fractions. Gangliosides were extracted, purified and analyzed by HPLC/MS as in Fig. 2. (C) Gangliosides extracted from undifferentiated (Day 0) and differentiated (Day 8) 3T3-L1 cells and RAW264 macrophage were separated on TLC as described in Materials and methods.

ion-trap MS. A variety of methods of analyzing gangliosides have been reported. Standard HPLC methods identify and quantify oligosaccharide moieties that are released from gangliosides by digestion with ceramide glycanase [12]. Enzymatic digestion of a ganglioside leads to loss of the structural information on its ceramide moiety and a drawback for quantitative works, i.e., a difficulty in determining enzymatic conditions to ensure quantitative recovery of digested sugar chains. Furthermore, this method includes multiple processing steps and is laborious. On the other hand, HPLC/MS can separate an individual ganglioside molecular species and identify its sugar sequence and the structure of its ceramide moiety. Very recently the methods with MS and tandem MS combined with reverse-phase HPLC were applied to determine ganglioside profiles of glioblastoma cells [13] and mouse brain [14].

Adipose tissue contained a huge amount of triglycerides, and gangliosides as minor components. In our hands simple solvent partition methods were not suitable for extracting ganglioside from adipose tissues for MS measurements, because significant amounts of non-polar impurities were contaminated in ganglioside fractions. Hence, we used an anion-exchange column for enriching and purifying gangliosides and then purified ganglioside fractions were subjected to saponification under mild alkaline conditions to remove triacylglycerols and phospholipids almost completely. This resulted in breaking minor ester modification, e.g., an O-acetyl linkage on sugar groups, leading to missing these slightly modified forms. However, the amide linkage in N-glycolylneuraminyl moiety is preserved and we found that adipose GM3 in genetic obese models and all a-series gangliosides more complex than GM3 increased in obese adipose tissues prefer N-glycolylneuraminyl species.

In genetic, and diet-induced obese mice, adipose tissues contained abundant GM2, GM1, and GD1a, compared with each control group. A fractionation study showed that these gangliosides were increased in both adipocyte and SV fractions (Fig. 4A and B). The adipocyte fractions contain mature adipocytes, whereas SV contains pre-adipocytes and interstitial cells including resident and infiltrated macrophages. In SV fraction, expression of macrophage marker genes CD68 and F4/80 were significantly elevated in severely obese KKAy mice (Fig. 3D), indicating increased macrophage infiltration into the obese adipose tissues. Macrophage cell line contained significantly higher amount of GM1 and GD1a, compared to pre-adipocytes and mature adipocytes, like SV (Fig 4C). These results suggest that infiltrated macrophage could take part in the increased GM1 and GD1a levels in SV fraction. A previous in vitro study showed that a proinflammatory cytokine TNFα elicited both GM3 synthase expression and activity in 3T3-L1 adipocytes, suggesting that TNFα secreted from infiltrated macrophages could have a regulatory role in ganglioside synthase expression [7]. In contrast, this study shows the mRNA levels of GM2 synthase were significantly increased in the adipose tissues of DIO and KKAy mice, but not those of GM3 synthase (Fig. 3A and C). This suggests that the action of GM2 synthase directs the metabolic flow of a-series ganglioside towards GD1a. The exact roles played by gangliosides and cytokines secreted by infiltrated macrophages in obesity pathophysiology remain to be clarified.

In both DIO and genetic obesity models, the proportion of GM3 species with shorter chain acyl (16:0 and 18:0) moieties significantly increased, compared with each control group. It has generally been accepted that GM3 is enriched in lipid microdomain. GM3 is the major adipose gangliosides (Fig. 2A) and can take part in forming a scaffold of lipid microdomain. Shortening of GM3 acyl moieties causes an increase in membrane fluidity of the domains, which may perturb its functional integrity, leading to affecting signaling efficiency through lipid microdomain. In this connection, T cell-specific targeting of serine palmitoyltransferase gene caused loss of sphingolipids and shortening of their acyl moieties in detergent-resistant membrane fractions prepared from targeted thymocytes, which is associated with abnormal T cell differentiation in the thymus (H. Tojo, S. Osuka, unpublished results).

In summary, we demonstrated that obesity induced adipose a-series gangliosides downstream of GM3: GM2, GM1, and GD1a by normal-phase HPLC/MS. Functional analysis of these gangliosides will shed light on the pathophysiology of obesity-associated diseases.

Acknowledgments

This work was supported by Grants-in-Aid for Scientific Research from the Ministry of Education, Culture, Sports, Science, and Technology of Japan, and Ono pharmaceutical Research Grant.

Appendix A. Supplementary data

Supplementary data associated with this article can be found, in the online version, at doi:10.1016/j.bbrc.2008.12.086.

References

[1] A.W. Ferrante Jr., Obesity-induced inflammation: a metabolic dialogue in the language of inflammation, J. Intern. Med. 262 (2007) 408–414.

[2] S.P. Weisberg, D. McCann, M. Desai, M. Rosenbaum, R.L. Leibel, A.W. Ferrante Jr., Obesity is associated with macrophage accumulation in adipose tissue, J. Clin. Invest. 112 (2003) 1796–1808.

[3] S.P. Weisberg, D. Hunter, R. Huber, J. Lemieux, S. Slaymaker, K. Vaddi, I. Charo, R.L. Leibel, A.W. Ferrante Jr., CCR2 modulates inflammatory and metabolic effects of high-fat feeding, J. Clin. Invest. 116 (2006) 115–124.

[4] G. Van Echten, K. Sandhoff, Ganglioside metabolism. Enzymology, topology, and regulation, J. Biol. Chem. 268 (1993) 5341–5344.

[5] S. Hakomori, Bifunctional role of glycosphingolipids. Modulators for transmembrane signaling and mediators for cellular interactions, J. Biol. Chem. 265 (1990) 18713–18716.

[6] T. Yamashita, A. Hashiramoto, M. Haluzik, H. Mizukami, S. Beck, A. Norton, M. Kono, S. Tsuji, J.L. Daniotti, N. Werth, R. Sandhoff, K. Sandhoff, R.L. Proia, Enhanced insulin sensitivity in mice lacking ganglioside GM3, Proc. Natl. Acad. Sci. USA 100 (2003) 3445–3449.

[7] S. Tagami, J. Inokuchi Ji, K. Kabayama, H. Yoshimura, F. Kitamura, S. Uemura, C. Ogawa, A. Ishii, M. Saito, Y. Ohtsuka, S. Sakaue, Y. Igarashi, Ganglioside GM3 participates in the pathological conditions of insulin resistance, J. Biol. Chem. 277 (2002) 3085–3092.

[8] T. Pacuszka, J. Moss, P.H. Fishman, A sensitive method for the detection of GM1-ganglioside in rat adipocyte preparations based on its interaction with choleragen, J. Biol. Chem. 253 (1978) 5103–5108.

[9] M. Ito, U. Tchoua, M. Okamoto, H. Tojo, Purification and properties of a phospholipase A2/lipase preferring phosphatidic acid, bis(monoacylglycerol) phosphate, and monoacylglycerol from rat testis, J. Biol. Chem. 277 (2002) 43674–43681.

[10] Y. Nagatsuka, H. Tojo, Y. Hirabayashi, Identification and analysis of novel glycolipids in vertebrate brains by HPLC/mass spectrometry, Methods Enzymol. 417 (2006) 155–167.

[11] S.K. Kundu, D.D. Scott, Rapid separation of gangliosides by high-performance liquid chromatography, J. Chromatogr. 232 (1982) 19–27.

[12] J.M. Aerts, R. Ottenhoff, A.S. Powlson, A. Grefhorst, M. van Eijk, P.F. Dubbelhuis, J. Aten, F. Kuipers, M.J. Serlie, T. Wennekes, J.K. Sethi, S. O'Rahilly, H.S. Overkleeft, Pharmacological inhibition of glucosylceramide synthase enhances insulin sensitivity, Diabetes 56 (2007) 1341–1349.

[13] H. He, C.A. Conrad, C.L. Nilsson, Y. Ji, T.M. Schaub, A.G. Marshall, M.R. Emmett, Method for lipidomic analysis: p53 expression modulation of sulfatide, ganglioside, and phospholipid composition of U87 MG glioblastoma cells, Anal. Chem. 79 (2007) 8423–8430.

[14] K. Ikeda, T. Shimizu, R. Taguchi, Targeted analysis of ganglioside and sulfatide molecular species by LC/ESI-MS/MS with theoretically expanded multiple reaction monitoring, J. Lipid Res. 49 (2008) 2678–2689.

JOURNAL OF PROTEOMICS XX (2009) XXX–XXX

available at www.sciencedirect.com

ScienceDirect

www.elsevier.com/locate/jprot

Journal of PROTEOMICS

Proteomic analysis of laser-microdissected paraffin-embedded tissues: (1) Stage-related protein candidates upon non-metastatic lung adenocarcinoma

Takeshi Kawamura[a,1], *Masaharu Nomura*[b,1], *Hiromasa Tojo*[c], *Kiyonaga Fujii*[d], *Hiroko Hamasaki*[e], *Sayaka Mikami*[f], *Yasuhiko Bando*[f], *Harubumi Kato*[b], *Toshihide Nishimura*[b,*,1]

[a] *Laboratory for Systems Biology and Medicine, RCAST, The University of Tokyo, Tokyo, Japan*
[b] *Department of Surgery I, Tokyo Medical University, Shinjuku, Tokyo, Japan*
[c] *Department of Biophysics and Biochemistry, Osaka University Graduate School of Medicine, Osaka, Japan*
[d] *Department of Structural Biology, Graduate School of Pharmaceutical Sciences, Hokkaido University, Sapporo, Japan*
[e] *Department of Biomedical Science, Graduate School of Agricultural and Life Sciences, The University of Tokyo, Tokyo, Japan*
[f] *Biosys Technologies, Inc., Meguro, Tokyo, Japan*

ARTICLE INFO

Article history:
Received 14 September 2009
Accepted 23 November 2009

Keywords:
Formalin-fixed paraffin-embedded tissue
Laser microdissection
Stage-related biomarkers
Lung adenocarcinoma
Mass spectrometry
Spectral counting

ABSTRACT

We used formalin-fixed paraffin-embedded (FFPE) materials for biomarker discovery in cases of lung cancer using proteomic analysis. We conducted a retrospective global proteomic study in order to characterize protein expression reflecting clinical stages of individual patients with stage I lung adenocarcinoma without lymph node involvement ($n=7$). In addition, we studied more advanced stage IIIA with spread to lymph nodes ($n=6$), because the degree of lymph node involvement is the most important factor for staging. FFPE sections of cancerous lesions resected surgically from patients with well-characterized clinical history were subjected to laser microdissection (LMD) followed by Liquid Tissue™ solubilization and digestion trypsin. Spectral counting was used to measure the amounts of proteins identified by shotgun liquid chromatography (LC)/tandem mass spectrometry (MS/MS). More than 500 proteins were identified from IA and IIIA cases, and non-parametric statistics showed that 81 proteins correlated significantly with stage IA or IIIA. A subset of those proteins were verified by multiple-reaction monitoring mass spectrometric quantitation (MRM assay), described in other paper in this issue. These results demonstrated the technical feasibility of a global proteomic study using clinically well documented FFPE sections, and its possible utility for detailed retrospective disease analyses in order to improve therapeutic strategy.

Abbreviations: FFPE, formalin-fixed paraffin-embedded; HE, hematoxylin and eosin; IHC, immunohistochemistry; ITMS, ion-trap mass spectrometer; LC, liquid chromatography; LMD, laser microdissection; MLN, mediastinal lymph nodes; MRM, multiple-reaction monitoring; MS, mass spectrometry; MS/MS, tandem mass spectrometry; NSAF, normalized spectral abundance factor; NSCLC, non-small cell lung cancer; NSI, nanoelectrospray ionization; SCLC, small cell lung cancers.

* *Corresponding author.* Department of Surgery I, Tokyo Medical University, 6-7-1 Nishishinjuku Shinjuku-ku, Tokyo 160-0023, Japan. Fax: +81 3 3340 0960.
E-mail address: linne300@aol.com (T. Nishimura).

[1] Contributed equally.

1874-3919/$ – see front matter © 2009 Elsevier B.V. All rights reserved.
doi:10.1016/j.jprot.2009.11.011

Please cite this article as: Kawamura T, et al, Proteomic analysis of laser-microdissected paraffin-embedded tissues: (1) Stage-related protein candidates upon non-metastatic lung adenocarcinoma, J Prot (2009), doi:10.1016/j.jprot.2009.11.011

1. Introduction

Lung cancer is one of the leading causes of cancer-related deaths worldwide [1–3]. Lung cancers are histologically classified into 2 major groups, non-small cell lung cancer (NSCLC), and small cell lung cancer (SCLC). NSCLC includes several subgroups such as adenocarcinoma, squamous cell carcinoma, and large cell carcinoma, and is more frequent than SCLC. A previous international study in 1997 reported that the 5-year survival rate of pathologic stage IA was 67%, while that of stage IIIA 23% [1]. Recent Japanese statistics in 2008 reported that the former considerably improved (83.9%), but not the latter (32.8%) [2]. The stage of lung cancer is related to prognosis, and the degree of cancer spread to lymph nodes is a critical component in the staging process [4]. It is therefore highly desirable to identify biomarkers that are differentially expressed in a stage-specific manner to help accurate staging.

Formalin-fixed and paraffin-embedded (FFPE) tissues have been extensively deposited in hospitals worldwide, together with detailed clinical records, e.g., disease history, clinical examination results, drug response and adverse reaction of individual patients, and are routinely used for diagnosis and staging of cancers by conventional staining, immunohistochemistry (IHC) [5] as well as *in situ* hybridization [6,7]. Recently emerging Liquid Tissue™ (Expression Pathology, Gaithersburg, MD, USA) technology has made it possible to extract proteins efficiently from FFPE tissues for proteomic analyses, providing a great opportunity for biomarker discovery using clinically archived FFPE tissues accompanied by both definitive diagnoses and known clinical outcomes [8–11]. We used spectral counting for peptide semi-quantification, which is a purely empirical approach based on sampling statistics [25,26]. While this method is still being developed and needs further experimental and statistical validation, it is suitable for analysis of low mass resolution LC/MS data and is feasible for large-scale human clinical proteomic studies [12].

We set out to determine the first successful application of shotgun LC/MS-based global proteomics to archived clinical FFPE specimen to identify stage-related biomarkers in cancer and lymph node tissues from stage IA and IIIA lung cancer.

2. Materials and methods

2.1. Tissues

Surgically removed lung and lymph node tissues were fixed with a buffered formalin solution containing 10–15% methanol, and embedded by a conventional method [13,14]. For stage IIIA, FFPE tissues of both primary lung lesions and involved lymph nodes were included. Archived paraffin blocks of formalin-fixed tissues obtained from 7 stage I and 6 stage IIIA lung cancer cases, which included well differentiated (W/D), moderate differentiated (M/D), and poorly differentiated (P/D) adenocarcinoma, were retrieved with the approval from Ethical Committee of Tokyo Medical University Hospital.

2.2. Materials

HPLC-grade acetonitrile and trifluoroacetic acid were purchased from Wako Pure Chemical Industries, Ltd. (Osaka, Japan). Milli-Q grade water (Millipore, Bedford, MA, USA) was used. Liquid Tissue MS Prep Kits and DIRECTOR™ slides were purchased from Expression Pathology (Gaithersburg, MD, USA).

2.3. Laser microdissection (LMD) and protein extraction

Cancerous lesions were identified on serial sections of NSCLC tissues stained with hematoxylin and eosin (HE). For proteomic analysis, a 10-μm thick section prepared from the same tissue block was attached onto DIRECTOR™ slides (Expression Pathology), de-paraffinized twice with xylene for 5 min, rehydrated with graded ethanol solutions and distilled water, and was then stained by only hematoxylin. Stained uncovered slides were air dried and ~30,000 cancerous cells (~1.2 mm^2) were collected into a 1.5-mL low-binding plastic tube using a Leica LMD6000 (Leica Microsystems GmbH, Ernst-Leitz-Strasse, Wetzlar, Germany). Protein extraction was performed using the Liquid Tissue™ MS Protein Prep kit according to the manufacturer's protocol (http://www.expressionpathology.com/).

2.4. Global LC-tandem MS and bioinformatic analysis of data

Peptide-mixture samples processed from FFPE tissues were used for nanoflow reverse phase liquid chromatography followed by tandem MS, using a LTQ linear ion-trap mass spectrometer (Thermo Fischer, San Jose, CA, USA).

A capillary reverse phase HPLC–MS/MS system (ZAPLOUS System™; AMR, Tokyo, Japan) composed of a Paradigm MS4 dual solvent delivery system (Michrom BioResources, Auburn, CA, USA), an HTC PAL autosampler (CTC Analytics, Zwingen, Switzerland), and Finnigan LTQ linear ion-trap mass spectrometers (ITMS; Thermo Fischer, San Jose, CA, USA) equipped with an XYZ nanoelectrospray ionization (NSI) source (AMR) [15–17]. The Liquid Tissue™ solvents were evaporated, and peptides were redissolved with MS-grade water containing 0.1% trifluoroacetic acid and 2% acetonitrile (solvent C). Aliquots of 10 μL (equivalent to 1 μg of proteins) were automatically injected into a peptide L-trap column (Chemical Evaluation Research Institute, Tokyo, Japan) attached to an injector valve for desalinating and concentrating peptides. After washing the trap with solvent C, the peptides were loaded into a separation capillary reverse phase column (MAGIC C18 packed with gel particles of 3 μm in diameter and 200-Å pore size, 50×0.1 mm, Michrom BioResources) by switching the valve. The eluents used were: A, 98% water/2% acetonitrile/0.1% formic acid, and B, 10% HR_2RO/90% acetonitrile/0.1% formic acid. The column was developed at a flow rate of ~0.5 μL/min with the concentration gradient of acetonitrile: from 5% B to 55% B in 100 min, then from 55% B to 95% B in 1 min, sustaining 95% B for 9 min, from 95% B to 5% B in 1 min, and finally re-equilibrating with 5% B for 9 min. Effluents were introduced into the mass spectrometer *via* the NSI interface that had a separation column outlet connected directly with an NSI needle (150-μm OD/20-μm ID FortisTip;

Please cite this article as: Kawamura T, et al, Proteomic analysis of laser-microdissected paraffin-embedded tissues: (1) Stage-related protein candidates upon non-metastatic lung adenocarcinoma, J Prot (2009), doi:10.1016/j.jprot.2009.11.011

OmniSeparo-TJ, Hyogo, Japan) [17]. The ESI voltage was 2.0 kV and the transfer capillary of the LTQ inlet was heated at 200 °C. No sheath or auxiliary gas was used. The mass spectrometer was operated in the *m/z* range of 450–2000 in a data-dependent acquisition mode, in which detecting the most abundant ions at a retention time automatically acquires MS/MS scans for those ions under the control of Xcalibur software (Thermo Fischer) with an isolation width of *m/z* 2.0 and a collisional activation amplitude of 35%. An MS scan sequence used was full-scan MS in the enhanced/profile mode, and sequential MS/MS in the normal/centroid mode, using dynamic exclusion capability, which allows sequential acquisition of MS/MS of abundant ions in the order of their intensities with an exclusion duration of 2.0 min and exclusion mass widths of −0.5 and +0.5 Da. The trapping time was 100 ms using the auto gain control.

All MS/MS spectral data were searched against the SwissProt 55.6 *Homo sapiens* database (20,009 entries) using Mascot (version_2.1.04, Matrix Science, London, UK) [18], in which the peptide and fragment mass tolerances were 2.0 Da and 0.8 Da [19–21], respectively. For variable peptide modifications, methionine oxidation, and *N*-formylation including formyl (K), formyl (R), and formyl (N-terminus) were taken into account. A *p*-value less than 0.05 was considered to indicate a statistically significant difference and the score cut-off was 44. Reported results were obtained from triplicate LC–MS runs for each sample with all peptide hit included. Unique peptides and proteins were determined by following the proteomics guidelines.

Scaffold (version 2.2.01; Proteome Software Inc., Portland, OR, USA) was utilized for the gene ontology analysis and validation of MS/MS-based peptide and protein identifications. Tandem mass spectra were extracted and deisotoped by BioWorks version 3.3 (Thermo Fischer, San Jose, CA, USA). Charge state deconvolution was not performed. For calculating spectral counts we used both Mascot and X! Tandem (version 2007.01.01.1) [22,23]. Peptide identifications were accepted if they could be established at greater than 95% probability as specified by the Peptide Prophet™ algorithm (Proteome Software, Portland OR, USA) [23]. Protein identifications were accepted if they could be established at greater than 95% probability and contained at least 1 identified peptide. Protein probabilities were assigned by the Protein Prophet™ algorithm (Institute for Systems Biology, Seattle, USA) [24]. Proteins which could not be differentiated by MS alone because of the presence of similar peptide sets in their digests were grouped according to the principle of parsimony.

To facilitate the biological interpretation of the extensive protein lists generated in the study, the proteins were classified in gene ontology categories, based on their biological processes and molecular and cellular functions.

2.5. *Spectral counting analysis of identified proteins*

Fold changes of expressed proteins in the base 2 logarithmic scale were calculated using the R_{SC} as defined by Old et al. [25] based upon spectral counting. Relative abundances of identified proteins were also obtained by using the normalized spectral abundance factor (NSAF) introduced by Zabailov et al. [26] Candidate proteins between groups were chosen so that their R_{SC} satisfy >1 or <−1, which correspond to their fold changes >2 or <0.5, and also statistical significance should be $p<0.05$ by either non-parametric *U*- or *G*-test [27].

3. Results

3.1. *NSCLC samples and laser microdissection*

To investigate the molecular profile of proteins expressed in relevance to early-stage NSCLC progression, we conducted a proteomic analysis of FFPE NSCLC tumors. Tissue tumors were classified by light microscopy of H&E-stained sections into stage IA (i.e., lacking involvement of mediastinal lymph nodes) or stage IIIA carcinoma (i.e., involvement of mediastinal lymph nodes) that were W/D, M/D, and P/D. They involved histological sub-classifications (bronchioloalveolar carcinoma (BAC), papillary adenocarcinoma (PAP), acinar adenocarcinoma and solid adenocarcinoma with mucin production). The stage I group consisted of 7 independent primary tumor samples, and the stage IIIA group of 6 independent sample sets in which one is from the primary tumor and another from a metastatic mediastinal lymph node. The pathological and clinical information are shown in Table 1. Patient characteristics were as follows: 4 women (31%) and 9 men (69%), with ages ranging from 43 to 74 (median, 63.6). All were adenocarcinoma: 8 were W/D (62%); 2 M/D (15%); and 3 were P/D (23%). The pathological stages: 6 were IA (T1N0M0) (46%); 1 IB (T2N0M0) (8%); and 6 were IIIA (T2N2M0) (46%). The workflow of global proteomics for the study is illustrated in Fig. 1, which is the combination of both laser microdissection and tandem MS. The methodology of laser microdissection adopted here is well suited for the rapid procurement of specific cell populations, which are collected directly onto caps, without any danger of handling contamination, for immediate processing and MS analysis. Laser microdissection considerably reduces sample complexity prior to MS analysis, and this platform results in a broad dynamic range of peptide measurements, which is advantageous for identification of diagnostically important proteins in lung adenocarcinoma as well as biomarkers for NSCLC progression.

3.2. *Protein identification and profile in IA and IIIA NSCLC*

Samples typically containing approximately 30,000 cells were processed as described in the Materials and methods. To compare protein expression across all tissue samples, we used the spectral counting method. Fig. 2 shows the Venn map for identified proteins ($p<0.05$). Under the search parameter settings used, proteins identified were respectively 449 (primary cancer lesions of stage IA), 438 (primary cancer lesions at stage IIIA), and 233 (metastatic mediastinal lymph nodes of stage IIIA). Among the total of 649 (100%) proteins identified from all primary lesions, 238 (36.8%) proteins were identified in both stages, while 211 (32.5%) and 200 (30.7%) proteins from primary lesions were unique to stage IA or IIIA, respectively. Among the total of 521 proteins (100%) characterizing both the stage IIIA primary and metastatic lesions, 288 (55.3%) proteins were identified in the lung lesion alone, only

Please cite this article as: Kawamura T, et al, Proteomic analysis of laser-microdissected paraffin-embedded tissues: (1) Stage-related protein candidates upon non-metastatic lung adenocarcinoma, J Prot (2009), doi:10.1016/j.jprot.2009.11.011